minerals

MDPI

Article

Geochronology, Geochemistry, and In Situ Sr-Nd-Hf Isotopic Compositions of a Tourmaline-Bearing Leucogranite in Eastern Tethyan Himalaya: Implications for Tectonic Setting and Rare Metal Mineralization

Yangchen Drolma, Kaijun Li, Yubin Li, Jinshu Zhang, Chengye Yang *, Gen Zhang, Ruoming Li and Duo Liu

School of Engineering, Tibet University, Lhasa 850000, China; yjzm0907@utibet.edu.cn (Y.D.)
* Correspondence: yangchengye@utibet.edu.cn

Abstract: Himalayan leucogranite is an excellent target for understanding the orogenic process of the India–Asia collision, but its origin and tectonic significance are still under debate. An integrated study of geochronology, geochemistry, and in situ Sr-Nd-Hf isotopes was conducted for a tourmaline-bearing leucogranite in the eastern Tethyan Himalaya using LA-ICP-MS, X-ray fluorescence spectroscopy, and ICP-MS and LA-MC-ICP-MS, respectively. LA-ICP-MS U-Pb dating of zircon and monazite showed that it was emplaced at ~19 Ma. The leucogranite had high SiO_2 and Al_2O_3 contents ranging from 73.16 to 73.99 wt.% and 15.05 to 15.24 wt.%, respectively. It was characterized by a high aluminum saturation index (1.14–1.19) and Rb/Sr ratio (3.58–6.35), which is characteristic of S-type granite. The leucogranite was enriched in light rare-earth elements (LREEs; e.g., La and Ce) and large ion lithophile elements (LILEs; e.g., Rb, K, and Pb) and depleted in heavy rare-earth elements (e.g., Tm, Yb, and Lu) and high field strength elements (HFSEs; e.g., Nb, Zr, and Ti). It was characterized by high I Sr (t) (0.7268–0.7281) and low ε Nd (t) (−14.6 to −13.2) and ε Hf (t) (−12.6 to −9.47), which was consistent with the isotopic characteristics of the Higher Himalayan Sequence. Petrogenetically, the origin of the leucogranite is best explained by the decompression-induced muscovite dehydration melting of an ancient metapelitic source within the Higher Himalayan Sequence during regional extension due to the movement of the South Tibetan Detachment System (STDS). The significantly high lithium and beryllium contents of the leucogranite and associated pegmatite suggest that Himalayan leucogranites possess huge potential for lithium and beryllium exploration.

Keywords: leucogranite; Sr-Nd-Hf isotopes; petrogenesis; South Tibetan Detachment System; rare-metal mineralization; Himalaya

Citation: Drolma, Y.; Li, K.; Li, Y.; Zhang, J.; Yang, C.; Zhang, G.; Li, R.; Liu, D. Geochronology, Geochemistry, and In Situ Sr-Nd-Hf Isotopic Compositions of a Tourmaline-Bearing Leucogranite in Eastern Tethyan Himalaya: Implications for Tectonic Setting and Rare Metal Mineralization. *Minerals* **2024**, *14*, 755. https://doi.org/10.3390/min14080755

Academic Editor: David Lentz

Received: 3 April 2024
Revised: 22 July 2024
Accepted: 24 July 2024
Published: 26 July 2024

1. Introduction

The Himalayan orogen, formed by the India–Asia collision, is the youngest continent–continent collisional orogen in the world [1,2]. With the development of the continental collision, extensive crustal melting shaped two Cenozoic E–W-trending leucogranite belts, i.e., the Tethyan Himalayan and Higher Himalayan belts, which serve as essential targets for comprehending the tectono-magmatic evolution of the Himalayan orogen [3–7]. Although many studies have been conducted on Himalayan leucogranites, their petrogenesis remains highly controversial. Many researchers have interpreted Himalayan leucogranites as a product of the partial melting of metasedimentary rocks, but recently, fractional crystallization has emerged as having a potentially key role in their formation [8–15]. Additionally, the source rocks and melting processes of these leucogranites are still debated [16–19], and the geodynamic processes responsible for their formation are also under discussion [20,21]. For example, some researchers consider the High Himalayan Sequence to represent the source of the leucogranites, while others suggest a two-component mixture between the Higher Himalayan Sequence and the Lesser Himalayan Sequence. Notably, rare-metal

mineralization has been discovered in almost all Himalayan leucogranites, with three large or giant rare-metal deposits found in the Himalayan metallogenic belt [22–24]. Thus, understanding the genesis and magmatic evolution process of Himalayan leucogranites is also helpful for extending ore deposit exploration.

This report describes in detail the zircon and monazite U-Pb dating, petrochemistry, and in situ Sr-Nd-Hf isotopic data related to a tourmaline-bearing leucogranite from the Luozha area in the eastern Tethyan Himalaya. These data were used to constrain the geochemical characteristics of the studied leucogranite. Together with previous studies, we decipher the petrogenesis of the tourmaline-bearing leucogranite and its tectonic and metallogenetic implications.

2. Geological Background

The Tibetan Plateau comprises multiple accretionary terranes, including the Himalayan, Lhasa, Qiangtang, and Songpan–Ganzi–Hoh–Xil terranes, which are separated by the Indus–Yarlung, Bangong–Nujiang, and Jinsha suture zones, respectively [1]. The Indus–Yarlung suture zone, in particular, was formed between the Lhasa and Himalayan terranes after the closure of the Tethys Ocean and contains numerous occurrences of ophiolite. The Himalayan terrane is characterized by widespread exposure of Precambrian metamorphic rocks and the development of virtually continuous marine strata from the Ordovician to the Neogene, comprising the Tethyan Himalaya Sequence, Greater Himalayan Sequence, Lesser Himalayan Sequence, and Sub-Himalayan Sequence [5]. Himalayan leucogranites are widely exposed in the Tethyan Himalayan and Higher Himalayan belts. The tourmaline-bearing leucogranite in this study is located in northern Luozha County, in the eastern Tethyan Himalayan belt, and is one of several leucogranites in this area (Figure 1). The Luozha tourmaline-bearing leucogranites (LTLGs) intruded the Early Carboniferous Guzi Formation, which is mainly composed of marble, mica schist, and andalusite–garnet–staurolite schist. Numerous pegmatites intruded the LTLGs and their country rocks, and two spodumene-bearing pegmatite zones were developed around the LTLGs (Figure 2).

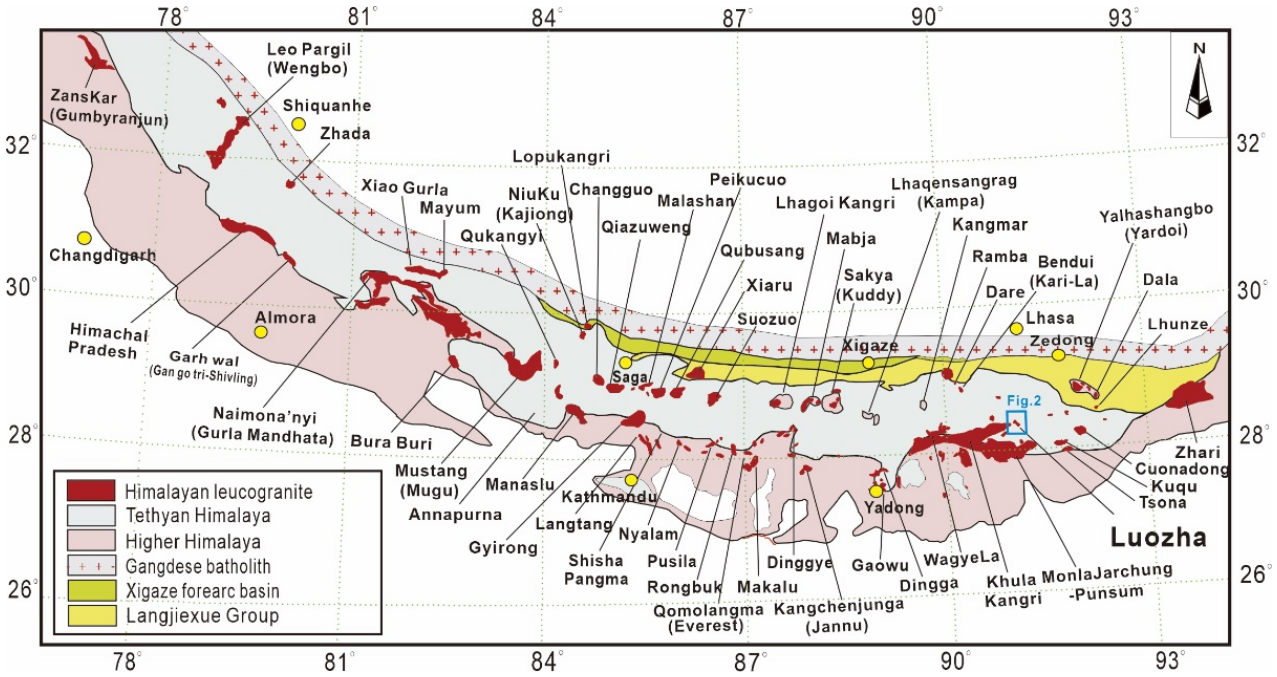

Figure 1. Geological sketch map of the Himalayas showing the distribution of Himalayan leucogranites (after [5]).

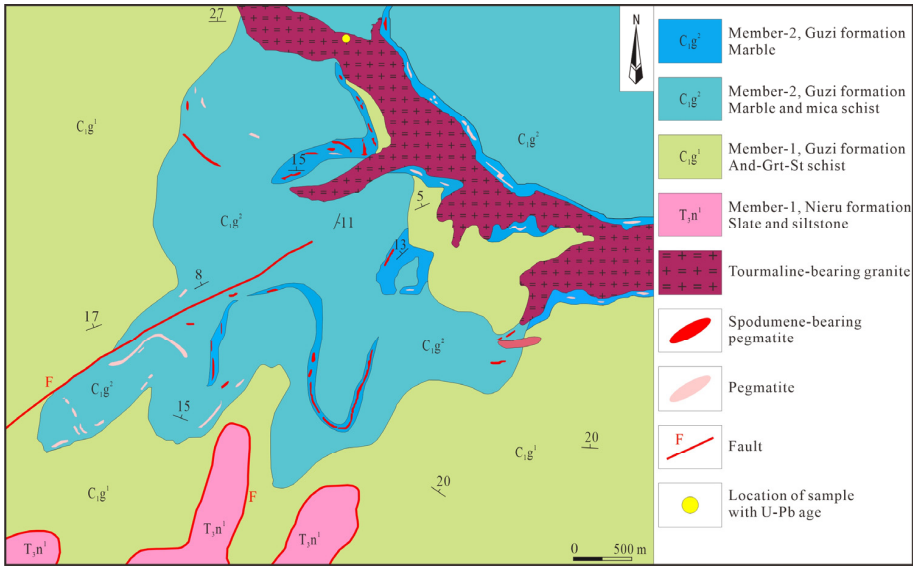

Figure 2. Simplified geological map of the Luozha tourmaline-bearing leucogranite (after [25]). Mineral abbreviations [26]: And, andalusite; Grt, garnet; St, staurolite.

3. Petrography

The Luozha tourmaline-bearing leucogranites (LTLGs) are light gray, medium-grained, and massive. Some rocks show oriented arrangements of tourmaline and platy minerals (Figure 3a). The main minerals are alkali feldspar (30%–35%), plagioclase (25%–35%), and quartz (25%–30%), with small amounts of tourmaline (3%–9%), muscovite (4%–7%), and biotite (<3%) (Figure 3b). The accessory minerals mainly include zircon, apatite, monazite, and magnetite. Rare-metal minerals such as beryl and spodumene are present in the pegmatites. Spodumene-bearing pegmatites consist mainly of alkali feldspar, plagioclase, quartz, and spodumene, with small amounts of garnet, muscovite, and tourmaline (Figure 3c,d).

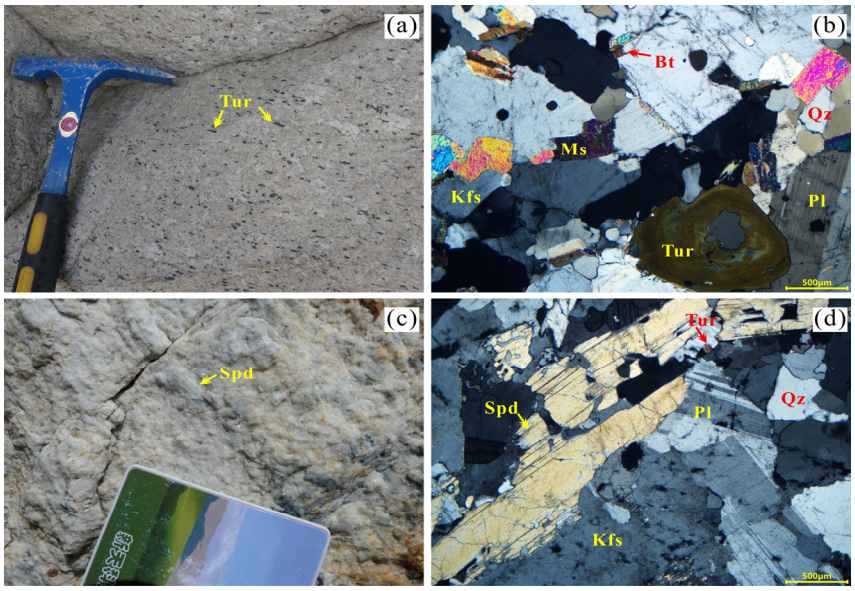

Figure 3. Representative field photographs and photomicrographs of the LTLG and spodumene-bearing pegmatites. (**a**) Field photograph showing oriented tourmalines of the LTLG; (**b**) Photomicrograph of the LTLG; (**c**) Field photograph of the spodumene-bearing pegmatite and (**d**) Photomicrograph of the spodumene-bearing pegmatite. Mineral abbreviations [26]: Bt, biotite; Kfs, K-feldspar; Ms, muscovite; Pl, plagioclase; Qz, quartz; Spd, Spodumene; Tur, tourmaline.

4. Materials and Methods

4.1. Materials

Eleven Luozha tourmaline-bearing leucogranite samples were acquired from unweathered outcrops in the field. Sample TGL01-4, intended for zircon and monazite U-Pb dating and an in situ Sr-Nd-Hf isotope study, underwent grinding to 40–60 mesh followed by elutriation, magnetic separation, electromagnetic separation, and heavy liquid beneficiation. Subsequently, the samples were examined to isolate zircon, monazite, and apatite grains. The 11 samples for geochemical analysis were crushed to less than 75 μm and divided into two portions to analyze the major oxides and trace elements.

4.2. Zircon and Monazite U-Pb Dating

U-Pb dating of zircon and monazite was performed with LA-ICP-MS by Wuhan Sample Solution Analytical Technology Co., Ltd., Wuhan, China, using a GeolasPro laser ablation system and Agilent 7900 ICP-MS instrument. In this study, the zircon analyses utilized a spot diameter of 32 μm at 5 Hz, while the monazite analyses used 16 μm at 2 Hz. Each analysis included a 20–30 s background acquisition followed by 50 s of sample data acquisition. Zircon 91500 and Monazite GBW44069 were used as external standards for zircon and monazite U-Pb dating, respectively. Isotope and trace element fractionation correction employed NIST610 glass as a reference material. The U-Pb dating data were processed by the Excel-based software ICPMSDataCal [27,28]. Isoplot/Ex_ver3 was used to create concordia diagrams and calculate weighted means [29].

4.3. Whole-Rock Major Oxides and Trace Elements Analysis

Major oxide analyses of whole rocks were conducted using a Zsx Primus II X-ray fluorescence spectrometer (XRF) equipped with a 4.0 kW end window Rh target X-ray tube at Wuhan Sample Solution Analytical Technology Co., Ltd., Wuhan, China. The operating conditions were set to a 50 kV voltage and a 60 mA current. Samples for the whole-rock major oxide analysis underwent pretreatment using the melting method. The flux consisted of lithium tetraborate–lithium metaborate–lithium fluoride (45:10:5), with ammonium nitrate as the oxidant and lithium bromide as the release agent. Melting was performed at 1050 °C for 15 min. The standard curve used the national standard material with an analytical precision better than 2 RSD% (the relative standard deviation).

Whole-rock trace elemental compositions were analyzed on an Agilent 7700e ICP-MS by Wuhan Sample Solution Analytical Technology Co., Ltd., Wuhan, China. Sample preparation involved the following steps: (1) drying 200-mesh samples in a 105 °C oven for 12 h; (2) weighing 50 mg of the powdered sample into a Teflon sample cartridge; (3) sequential addition of 1 mL of high-purity HNO_3 and 1 mL of high-purity HF; (4) placing the Teflon sample bomb into a stainless steel pressure jacket, sealing it, and heating it in an oven at 190 °C for more than 24 h; (5) cooling the dissolved sample, opening the lid, and steaming on a 140 °C electric heating plate, followed by addition of 1 mL of HNO_3 and steaming again; (6) adding 1 mL of high-purity HNO_3, 1 mL of MQ water, and 1 mL of internal standard In (concentration of 1 ppm), and then placing the dissolved Teflon sample bomb back into the steel sleeve, sealing it, and heating it in an oven at 190 °C for over 12 h; (7) transferring the solution into a polyethylene feed bottle and diluting to 100 g with 2% HNO_3 for testing. The detailed analysis procedure follows the "Methods for Chemical Analysis of Silicate Rocks—Part 30: Determination of 44 Elements" in the standard GB/T14506.30-2010 [30]. The external standards were based on the rock standards BHVO-2, GSR-1, and GSR-3, and the analysis precision was generally better than 10%.

4.4. In Situ Sr-Nd-Hf Isotopic Analysis

In situ Sr isotope ratios of apatites, Nd isotopes of apatite and monazite microregions, and Hf isotopes of zircons were analyzed using a Neptune Plus MC-ICP-MS (Thermo Fisher Scientific, Bremen, Germany) in combination with a Geolas HD excimer ArF laser ablation system (Coherent, Göttingen, Germany) by Wuhan Sample Solution Analytical

Technology Co., Ltd., Wuhan, China. Each measurement involved a 20 s acquisition of background signals followed by 50 s of ablation signal acquisition. All analytical data were processed using Iso-Compass (China University of Geosciences, Wuhan, China), a specialized isotope data processing software [31].

Regarding the laser ablation of Sr, a spot diameter of 90 μm and a pulse frequency of 8 Hz were employed. Laser fluence was maintained at approximately 10 J/cm^2. The Faraday collector configuration of the mass spectrometer included an array from L4 to H3 to monitor Kr, Rb, Er, Yb, and Sr. $^{88}Sr/^{86}Sr = 8.375209$ was used as a reference for correcting the mass fractionation of Sr isotopes. Interference correction followed the strategies detailed by Tong et al. [32] and Zhang et al. [33]. Two natural apatites, Durango and MAD, served as unknown samples for the in situ Sr isotope analysis, with their chemical and isotopic compositions previously reported by Yang et al. [34].

For the single-laser spot ablation of Nd, the spot diameter was set at 90 μm with a pulse frequency of 8 Hz for apatite and 24 μm with a pulse frequency of 2 Hz for monazite. The laser fluence remained constant at approximately 8 J/cm^2. The mass spectrometer simultaneously detected ^{142}Nd, ^{143}Nd, ^{144}Nd, ^{145}Nd, ^{146}Nd, ^{147}Sm, ^{148}Nd, and ^{149}Sm isotopes. Following interference corrections, the mass fractionation of Nd isotopes was adjusted using $^{146}Nd/^{144}Nd = 0.7219$ as the standard ratio. Detailed methodology can be found in Xu et al.'s study [35].

For the analysis of in situ Hf isotopes, a single-spot ablation mode with a 44 μm spot size was employed. The laser ablation energy density was 7 J/cm^2. We utilized the βYb value directly obtained from the zircon sample itself in real time for this study. To ensure the reliability of the analytical data, three international zircon standards—Plešovice, 91500, and GJ-1—were simultaneously analyzed alongside the actual samples. Their isotopic compositions are noted and described by Zhang et al. [31].

5. Results

5.1. Zircon and Monazite U-Pb Ages

The zircon grains from sample TGL01-4 were mostly euhedral, transparent, and colorless. The zircons used for the U-Pb dating were generally prismatic and ranged in size from 100 to 300 μm with length/width ratios of 2:1 to 4:1. Most zircons exhibited oscillatory zoning and a bubbly or clearly core–rim structure (Figure 3a). The zircon rims also showed well-developed oscillatory zoning, indicating a magmatic origin [36], and inherited cores often had no or weak, planar, or oscillatory zoning (Figure 4a). The results of the zircon U-Pb dating are shown in Table 1. Among the 17 analytical spots on 16 zircon grains, one analysis of inherited cores obtained 207Pb/206Pb ages of 1993 ± 46 Ma, but other inherited cores were too small to achieve a reliable result (Figure 4b). Sixteen analyses on magmatic rims and bubbly grains yielded 206Pb/238U ages of 19.4–18.1 Ma, with a weighted mean age of 18.66 ± 0.16 Ma (MSWD = 2.6) (Figure 4c). The Ti content of magmatic zircons ranged from 2.33 to 13.1 ppm, and the calculated Ti-in-zircon temperatures ranged from 627 to 765 °C [37], with an average of 685 °C.

The monazite grains from Sample TGL01-4 were generally subhedral and stubby prismatic. Most grains showed weakly oscillatory zoning ranging in size from 40 to 100 μm. The results of the monazite U-Pb dating are shown in Table 2. Fourteen analyses of 14 monazite grains yielded 206Pb/238U ages of 19.3–18.0 Ma, with a weighted mean age of 18.59 ± 0.22 Ma (MSWD = 1.4) (Figure 4d), which is consistent with the age of magmatic zircon.

Table 1. LA-ICP-MS U-Pb isotopic data and Ti-in-zircon temperatures for zircon from the LTLG.

Spot	Th	U	Ti	Th/U	TTi-in-zircon	207Pb/206Pb		207Pb/235U		206Pb/238U		207Pb/206Pb		207Pb/235U		206Pb/238U	
						Ratio	1 s	Ratio	1 s	Ratio	1 s	Age	1 s	Age	1 s	Age	1 s
TGL01-4Z-01	424	9884	8.06	0.04	722	0.0463	0.0018	0.0184	0.0007	0.0029	0.0000	12	78	18.5	0.7	18.5	0.2
TGL01-4Z-02	341	10,156	4.25	0.03	671	0.0494	0.0017	0.0198	0.0007	0.0029	0.0000	168	81	19.9	0.7	18.5	0.2
TGL01-4Z-03	308	4642	8.86	0.07	730	0.0521	0.0022	0.0214	0.0009	0.0030	0.0000	289	94	21.5	0.9	19.0	0.2
TGL01-4Z-04	254	10,156	-	0.02		0.0475	0.0015	0.0189	0.0005	0.0029	0.0000	76	63	19	0.5	18.5	0.2
TGL01-4Z-05	879	23,739	5.97	0.04	698	0.0538	0.0013	0.0226	0.0008	0.0030	0.0001	85	95	19.8	0.7	19.2	0.4
TGL01-4Z-06	3206	7793	-	0.41		0.0554	0.0019	0.0223	0.0007	0.0029	0.0000	428	74	22.4	0.7	18.6	0.2
TGL01-4Z-07	524	9968	13.1	0.05	765	0.0463	0.0015	0.0187	0.0006	0.0029	0.0000	15	66	18.8	0.6	18.7	0.2
TGL01-4Z-08	617	23,710	2.76	0.03	639	0.0483	0.0011	0.0193	0.0004	0.0029	0.0000	115	52	19.4	0.4	18.6	0.2
TGL01-4Z-09	146	4418	2.84	0.03	641	0.0488	0.0020	0.0195	0.0008	0.0029	0.0000	136	93	19.6	0.8	18.6	0.2
TGL01-4Z-10	718	21,044	8.86	0.03	730	0.1225	0.0034	5.7557	0.1545	0.3395	0.0031	1993	46	1940	23	1884	15
TGL01-4Z-11	71.8	4772	6.59	0.02	706	0.0509	0.0020	0.0198	0.0008	0.0028	0.0000	100	87	18.7	0.7	18.0	0.2
TGL01-4Z-12	315	6443	3.45	0.05	655	0.0478	0.0015	0.0196	0.0006	0.0030	0.0000	88	70	19.7	0.6	19.0	0.2
TGL01-4Z-13	231	8303	2.33	0.03	627	0.0497	0.0015	0.0201	0.0006	0.0029	0.0000	181	69	20.2	0.6	18.7	0.2
TGL01-4Z-14	268	13,532	5.96	0.02	697	0.0543	0.0014	0.0220	0.0006	0.0029	0.0000	66	67	19	0.5	18.6	0.2
TGL01-4Z-15	548	13,776	-	0.04		0.0471	0.0012	0.0192	0.0005	0.0029	0.0000	55	54	19.3	0.5	18.9	0.2
TGL01-4Z-16	327	9733	-	0.03		0.0462	0.0015	0.0189	0.0006	0.0030	0.0000	7	64	19.1	0.6	19.1	0.2
TGL01-4Z-17	93.4	5536	4.38	0.02	673	0.0479	0.0021	0.0186	0.0008	0.0028	0.0000	95	94	18.7	0.8	18.1	0.2

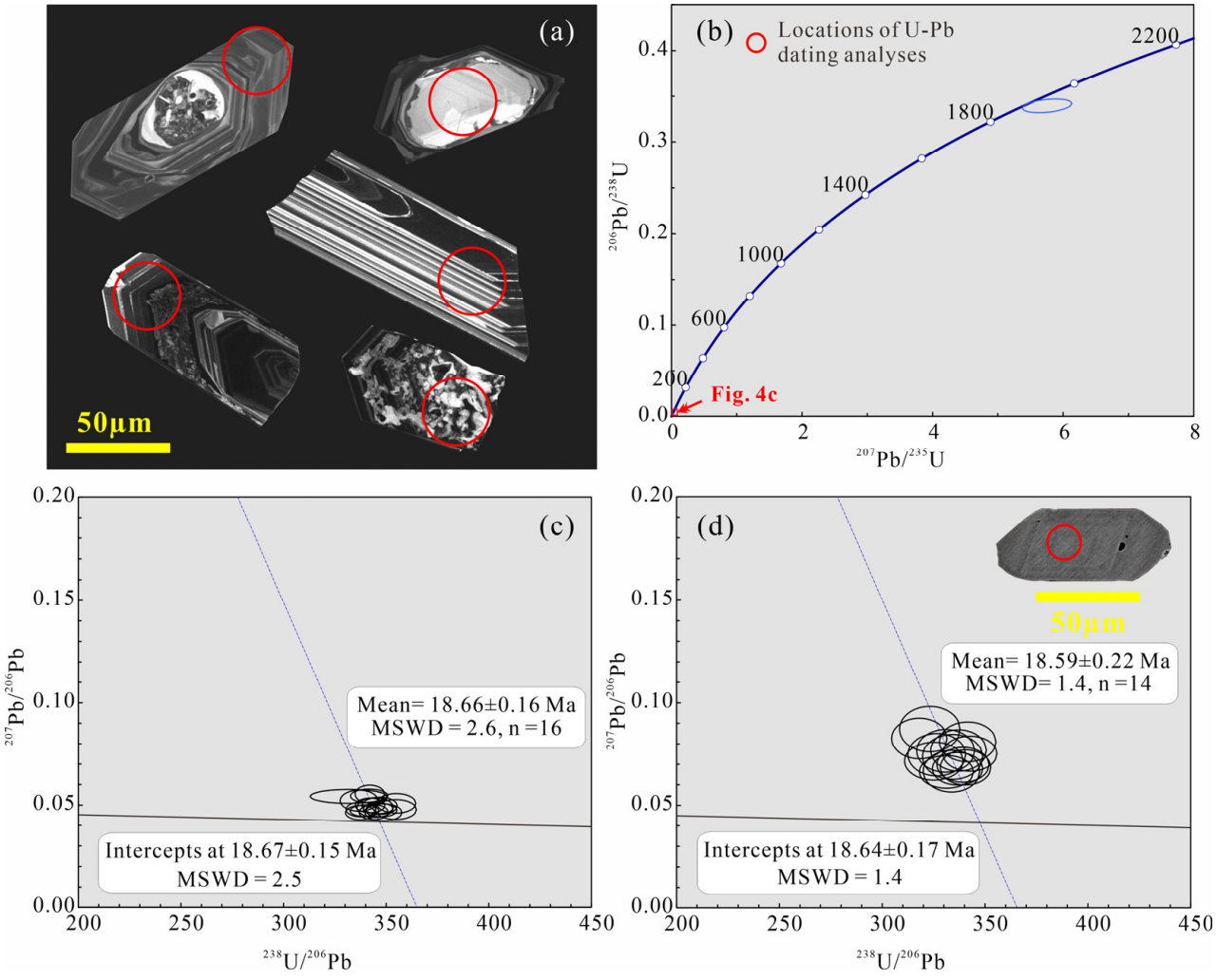

Figure 4. U-Pb dating results of the LTLG. (**a**) Cathodoluminescence images for representative zircons from the LTLG; (**b**) U-Pb zircon concordia diagram of the LTLG; Tera–Wasserburg concordia diagram for zircons (**c**) and monazites (**d**) of the LTLG. The red circle indicate the location of U-Pb dating analysis.

Table 2. LA-ICP-MS U-Pb isotopic data for monazite from the LTLG.

Spot	Th	U	Th/U	207Pb/206Pb		207Pb/235U		206Pb/238U		207Pb/235U		206Pb/238U		208Pb/232Th	
				Ratio	1 s	Ratio	1 s	Ratio	1 s	Age	1 s	Age	1 s	Age	1 s
TGL01-4M-01	62,701	9647	6.50	0.0663	0.0032	0.0276	0.0014	0.0030	0.0000	27.6	1.4	18.9	0.3	18.3	0.2
TGL01-4M-02	73,408	4923	14.91	0.0798	0.0053	0.0319	0.0019	0.0030	0.0001	31.9	1.8	18.6	0.3	18.9	0.2
TGL01-4M-03	83,213	8999	9.25	0.0691	0.0038	0.0278	0.0014	0.0030	0.0000	27.8	1.4	18.6	0.3	18.4	0.2
TGL01-4M-04	71,771	4699	15.27	0.0729	0.0042	0.0303	0.0017	0.0031	0.0001	30.4	1.7	19.1	0.4	18.7	0.2
TGL01-4M-05	79,742	7001	11.39	0.0767	0.0043	0.0303	0.0015	0.0029	0.0000	30.3	1.5	18.1	0.3	18.4	0.2
TGL01-4M-06	75,073	7379	10.17	0.0691	0.0037	0.0277	0.0015	0.0029	0.0000	27.8	1.4	18.4	0.3	18.5	0.2
TGL01-4M-07	64,482	4101	15.72	0.0764	0.0048	0.0315	0.0019	0.0031	0.0001	31.5	1.8	19.0	0.3	17.9	0.2
TGL01-4M-08	77,132	6874	11.22	0.0709	0.0040	0.0283	0.0015	0.0029	0.0000	28.4	1.5	18.4	0.3	18.4	0.2
TGL01-4M-09	74,297	5652	13.14	0.0777	0.0045	0.0314	0.0018	0.0030	0.0000	31.4	1.7	18.3	0.3	18.2	0.2
TGL01-4M-10	86,244	4800	17.97	0.0841	0.0046	0.0358	0.0019	0.0031	0.0001	35.7	1.8	19.3	0.4	18.1	0.2
TGL01-4M-11	88,744.0	5447	16.29	0.0818	0.0045	0.0327	0.0017	0.0029	0.0000	32.6	1.7	18.0	0.3	18.1	0.2
TGL01-4M-12	52,578	4041	13.01	0.0672	0.0047	0.0275	0.0018	0.0030	0.0001	27.6	1.7	18.8	0.3	18.8	0.2
TGL01-4M-13	53,956	3573	15.10	0.0741	0.0048	0.0304	0.0019	0.0030	0.0001	30.4	1.9	18.6	0.3	17.8	0.2
TGL01-4M-14	74,487	3672	20.29	0.0894	0.0054	0.0372	0.0021	0.0031	0.0001	37.1	2.0	18.8	0.4	18.2	0.2

5.2. Whole-Rock Major Oxides and Trace Elements

The major oxide and trace element results for the 11 Luozha tourmaline-bearing leucogranite samples are shown in Table 3. Samples TGL01-2, TGL01-3, TGL01-4, and TGL04-1 were obtained from the northwestern part of the Luozha pluton; samples TGL05-2, TGL06-1, TGL07-1, and TGL07-3 were from the middle of the Luozha pluton; samples TGL09-1, TGL10, and TGL11 were from the southeastern part of the Luozha pluton. The LTLG samples showed concentrated and high SiO_2 contents of 73.16 to 73.99 wt.% and were enriched in alkalis, with $Na_2O + K_2O$ contents between 8.07 and 8.68 wt.%. All samples plot within the granite field (Figure 5a). The samples had low CaO contents of 0.80–1.22 wt.%, which classifies these leucogranites as belonging to the alkali–calcic and calc-alkalic series (Figure 5b). All of the leucogranite samples were K-rich, with K_2O/Na_2O greater than 1.11 except for one at 0.97, and plotted within the high-K calc-alkaline series field (Figure 5c). They were characterized by low contents of TiO_2 (0.052–0.095 wt.%), $Fe_2O_3{}^t$ (total Fe oxides, shown as Fe_2O_3; $\leq$0.92 wt.%), MgO (0.11–0.20 wt.%), and MnO (0.010–0.025 wt.%). All of the leucogranite samples were corundum-normative and had high Al_2O_3 contents ranging from 15.05 to 15.24 wt.%. The samples were strongly peraluminous with a high aluminum saturation index (A/CNK) [molar $Al_2O_3/(CaO + Na_2O + K_2O)$] of 1.14–1.19 (Figure 5d).

In general, the LTLG samples shared similar features in their enrichments in light rare earth elements (LREEs; e.g., La and Ce) and large ion lithophile elements (LILEs; e.g., Rb, K, and Pb), as well as depletions in heavy rare earth elements (HREEs; e.g., Tm, Yb, and Lu) and high field strength elements (HFSEs; e.g., Nb, Zr, and Ti) (Figure 6). The samples revealed low concentrations of Sr (65.1–127 ppm), Zr (34.2–50.7 ppm), and Ba (103–222 ppm) and high Rb (338–454 ppm) concentrations, with variable Nb/Ta (5.92–15.9) and similar Zr/Hf (22.0–25.8) ratios. All of the leucogranites sampled have low total REE concentrations (48.4–78.5 ppm) and exhibit patterns enriched in LREEs and depleted in HREEs with high (La/Yb) N ratios (17.7–32.5, with an average of 27.1) in the chondrite-normalized rare earth element (REE) diagrams (Figure 6a). The samples showed moderately negative Eu anomalies (Eu/Eu* = 0.49–0.76) and a lack of notable lanthanide tetrad effects. In the primitive-mantle-normalized spider diagrams, all samples showed enrichment in LILEs, such as Rb and Th, with negative anomalies for Ba, Nb, Ta, Sr, P, Zr, and Ti (Figure 6b). Zircon saturation temperatures (T_{Zr}) of the leucogranites were calculated to estimate the temperatures of zircon crystallization, which yielded values of 677–703 °C [38], with an average of 686 °C. This average coincides with the average of the calculated Ti-in-zircon temperatures.

Table 3. Whole-rock major elements and trace elements of the TLTG.

Sample	TGL01-2	TGL01-3	TGL01-4	TGL04-1	TGL05-2	TGL06-1	TGL07-1	TGL07-3	TGL09-1	TGL10	TGL11	Average	Minimum	Maximum
Rock type	Tourmaline-bearing leucogranite													
Major element (wt.%)														
SiO2	73.16	73.90	73.82	73.57	73.63	73.79	73.99	73.41	73.35	73.46	73.76	73.62	73.16	73.99
TiO2	0.079	0.066	0.069	0.077	0.052	0.079	0.069	0.056	0.095	0.084	0.081	0.07	0.05	0.10
Al2O3	15.16	15.24	15.08	15.12	15.12	15.05	15.15	15.10	15.21	15.14	15.13	15.14	15.05	15.24
TFe2O3	0.83	0.78	0.71	0.78	0.64	0.80	0.80	0.75	0.78	0.82	0.83	0.78	0.64	0.83
MnO	0.011	0.010	0.012	0.012	0.010	0.021	0.020	0.015	0.025	0.014	0.015	0.01	0.01	0.02
MgO	0.12	0.12	0.12	0.15	0.12	0.15	0.12	0.11	0.20	0.16	0.14	0.14	0.11	0.20
CaO	0.97	0.85	0.92	0.92	0.80	0.96	0.93	0.95	1.22	1.03	1.02	0.96	0.80	1.22
Na2O	3.97	3.81	3.81	3.64	4.15	3.73	3.86	3.82	4.09	3.61	3.57	3.82	3.57	4.15
K2O	4.41	4.85	4.87	4.64	4.28	4.72	4.46	4.60	3.98	4.64	4.65	4.55	3.98	4.87
P2O5	0.10	0.09	0.10	0.08	0.08	0.09	0.08	0.09	0.08	0.10	0.10	0.09	0.08	0.10
LOI	0.43	0.46	0.37	0.54	0.53	0.74	0.69	0.59	0.68	0.62	0.61	0.57	0.37	0.74
SUM	99.24	100.18	99.88	99.52	99.41	100.11	100.17	99.48	99.72	99.68	99.91	99.75	99.24	100.18
Trace element (ppm)														
Li	34.1	68.4	152	220	63.5	34.8	409	294	499	303	332	219	34.1	499
Be	11.2	12.9	14.0	15.9	14.6	18.0	19.5	13.7	21.1	15.7	16.0	15.7	11.2	21.1
Sc	1.77	1.47	1.51	1.40	0.98	1.29	1.37	1.00	1.34	1.26	1.54	1.36	0.98	1.77
V	2.35	2.22	2.05	2.05	2.42	2.04	1.67	1.14	6.95	1.74	1.59	2.39	1.14	6.95
Cr	0.88	0.80	0.58	0.76	0.69	0.87	0.46	0.22	3.28	0.28	0.54	0.85	0.22	3.28
Co	0.48	0.42	0.39	0.53	0.34	0.47	0.33	0.33	0.74	0.43	0.47	0.45	0.33	0.74
Ni	0.65	0.43	0.35	0.36	0.30	0.40	0.14	0.18	1.20	0.21	0.34	0.41	0.14	1.20
Cu	0.81	0.72	0.51	0.58	1.10	0.49	0.37	0.34	0.42	0.40	0.37	0.56	0.34	1.10
Zn	50.4	60.7	48.2	53.1	43.7	44.1	55.1	51.1	55.2	54.8	50.0	51.5	43.7	60.7
Ga	33.2	29.6	29.9	31.3	25.6	30.2	33.9	31.9	27.5	33.7	31.3	30.8	25.6	33.9
Rb	382	435	427	395	338	393	444	417	454	380	372	403	338	454
Sr	84.7	71.0	74.3	74.5	69.2	78.7	70.0	70.1	127	86.5	84.7	81.0	69.2	127
Y	6.44	5.45	6.10	6.13	7.85	6.51	5.93	6.68	6.27	5.74	7.14	6.39	5.45	7.85
Zr	39.7	34.8	40.0	38.4	40.6	39.2	34.2	35.1	50.7	40.2	38.6	39.2	34.2	50.7
Nb	9.51	8.52	7.84	8.02	2.99	10.6	13.0	9.82	9.30	8.42	9.49	8.87	2.99	13.0
Sn	10.0	8.74	7.60	11.6	10.3	15.6	20.0	15.2	11.7	15.7	14.1	12.8	7.60	20.0
Cs	15.2	14.2	12.8	41.2	85.8	60.5	77.0	57.7	97.2	56.8	56.6	52.3	12.8	97.2
Ba	173	163	139	161	124	173	135	103	222	138	160	154	103	222
La	13.8	9.87	12.1	12.6	12.2	9.15	11.6	9.45	14.6	13.4	13.5	12.0	9.15	14.6
Ce	30.2	21.5	26.6	27.2	26.3	19.9	25.5	20.8	31.2	29.3	29.7	26.2	19.9	31.2
Pr	3.49	2.47	2.98	3.08	3.03	2.32	2.90	2.39	3.60	3.37	3.42	3.00	2.32	3.60

Table 3. *Cont.*

Sample	TGL01-2	TGL01-3	TGL01-4	TGL04-1	TGL05-2	TGL06-1	TGL07-1	TGL07-3	TGL09-1	TGL10	TGL11	Average	Minimum	Maximum
Nd	12.4	8.72	10.6	11.1	10.3	8.26	10.2	8.47	12.7	12.3	12.2	10.7	8.26	12.7
Sm	3.94	2.86	3.65	3.69	3.35	2.64	3.33	3.12	3.32	3.97	4.03	3.44	2.64	4.03
Eu	0.68	0.54	0.56	0.59	0.51	0.63	0.58	0.50	0.64	0.65	0.66	0.59	0.50	0.68
Gd	3.42	2.38	2.91	2.84	2.99	2.45	2.98	2.75	2.69	3.06	3.31	2.89	2.38	3.42
Tb	0.46	0.35	0.43	0.40	0.42	0.35	0.38	0.36	0.35	0.37	0.43	0.39	0.35	0.46
Dy	1.83	1.43	1.59	1.51	1.87	1.60	1.51	1.60	1.53	1.48	1.82	1.62	1.43	1.87
Ho	0.23	0.19	0.23	0.22	0.28	0.22	0.20	0.21	0.21	0.19	0.24	0.22	0.19	0.28
Er	0.45	0.39	0.45	0.46	0.59	0.45	0.41	0.49	0.42	0.43	0.54	0.46	0.39	0.59
Tm	0.051	0.040	0.048	0.052	0.080	0.057	0.046	0.059	0.054	0.049	0.065	0.05	0.04	0.08
Yb	0.30	0.26	0.28	0.31	0.50	0.31	0.28	0.36	0.33	0.30	0.38	0.33	0.26	0.50
Lu	0.039	0.035	0.040	0.044	0.067	0.042	0.036	0.045	0.040	0.037	0.050	0.04	0.04	0.07
Hf	1.74	1.50	1.82	1.64	1.73	1.68	1.54	1.56	1.97	1.65	1.56	1.67	1.50	1.97
Ta	0.60	0.77	0.71	0.99	0.46	1.47	1.15	1.48	1.57	1.09	1.47	1.07	0.46	1.57
Tl	2.25	2.67	2.46	2.21	1.97	2.18	2.58	2.47	2.93	2.23	2.19	2.38	1.97	2.93
Pb	89.8	94.3	98.7	91.0	88.8	96.1	85.5	92.2	83.0	86.7	95.7	91.1	83.0	98.7
Th	7.66	5.84	7.26	7.81	6.86	7.93	7.07	5.46	9.09	7.37	8.04	7.31	5.46	9.09
U	3.16	10.1	9.56	11.5	8.38	4.29	12.0	3.68	17.9	2.72	6.40	8.15	2.72	17.9
CIPW Norms														
Q	31.11	31.07	30.88	32.51	31.42	31.72	32.19	31.56	31.47	32.36	32.83	31.7	30.9	32.8
C	2.36	2.40	2.10	2.62	2.41	2.27	2.48	2.33	2.16	2.56	2.61	2.39	2.10	2.62
Ab	34.00	32.31	32.41	31.14	35.51	31.78	32.86	32.67	34.96	30.86	30.41	32.6	30.4	35.5
An	4.19	3.64	3.96	4.11	3.53	4.25	4.11	4.24	5.58	4.52	4.46	4.23	3.53	5.58
Or	26.45	28.82	28.99	27.81	25.62	28.13	26.57	27.52	23.84	27.73	27.76	27.2	23.8	29.0
Hy	1.34	1.28	1.17	1.33	1.11	1.36	1.32	1.24	1.47	1.41	1.38	1.31	1.11	1.47
Il	0.15	0.13	0.13	0.15	0.10	0.15	0.13	0.11	0.18	0.16	0.16	0.14	0.10	0.18
Mt	0.15	0.14	0.12	0.14	0.11	0.14	0.14	0.13	0.14	0.14	0.15	0.14	0.11	0.15
Ap	0.24	0.21	0.23	0.19	0.18	0.20	0.20	0.20	0.20	0.24	0.24	0.21	0.18	0.24
Zr/Ti	0.08	0.09	0.10	0.08	0.13	0.08	0.08	0.10	0.09	0.08	0.08	0.09	0.11	0.09
Na2O + K2O	8.38	8.66	8.68	8.29	8.42	8.45	8.32	8.41	8.07	8.25	8.22	8.38	8.07	8.68
K2O/Na2O	1.11	1.27	1.28	1.28	1.03	1.26	1.16	1.20	0.97	1.28	1.30	1.20	0.97	1.30
A/CNK	1.16	1.17	1.14	1.19	1.17	1.16	1.18	1.16	1.15	1.18	1.19	1.17	1.14	1.19
A/NK	1.34	1.32	1.31	1.37	1.32	1.34	1.36	1.34	1.38	1.38	1.39	1.35	1.31	1.39
Al2O3/TiO2	192	232	220	197	291	191	221	269	159	180	186	213	159	291
CaO/Na2O	0.24	0.22	0.24	0.25	0.19	0.26	0.24	0.25	0.30	0.29	0.29	0.25	0.19	0.30
Nb/Ta	15.9	11.1	11.0	8.06	6.52	7.22	11.3	6.65	5.92	7.72	6.44	8.90	5.92	15.9

Table 3. *Cont.*

Sample	TGL01-2	TGL01-3	TGL01-4	TGL04-1	TGL05-2	TGL06-1	TGL07-1	TGL07-3	TGL09-1	TGL10	TGL11	Average	Minimum	Maximum
Zr/Hf	22.8	23.2	22.0	23.4	23.5	23.3	22.2	22.5	25.8	24.3	24.7	23.4	22.0	25.8
(La/Yb)N	32.5	27.7	31.4	29.1	17.7	20.9	30.2	19.0	31.3	32.4	25.6	27.1	17.7	32.5
δEu	0.57	0.63	0.52	0.56	0.49	0.76	0.56	0.52	0.65	0.57	0.55	0.58	0.49	0.76
Rb/Sr	4.51	6.13	5.75	5.30	4.89	4.99	6.35	5.95	3.58	4.40	4.39	5.11	3.58	6.35
Rb/Ba	2.21	2.68	3.08	2.45	2.72	2.27	3.28	4.05	2.05	2.75	2.32	2.72	2.05	4.05
TZr (°C)	686	677	686	686	689	686	677	678	703	689	686	686	677	703

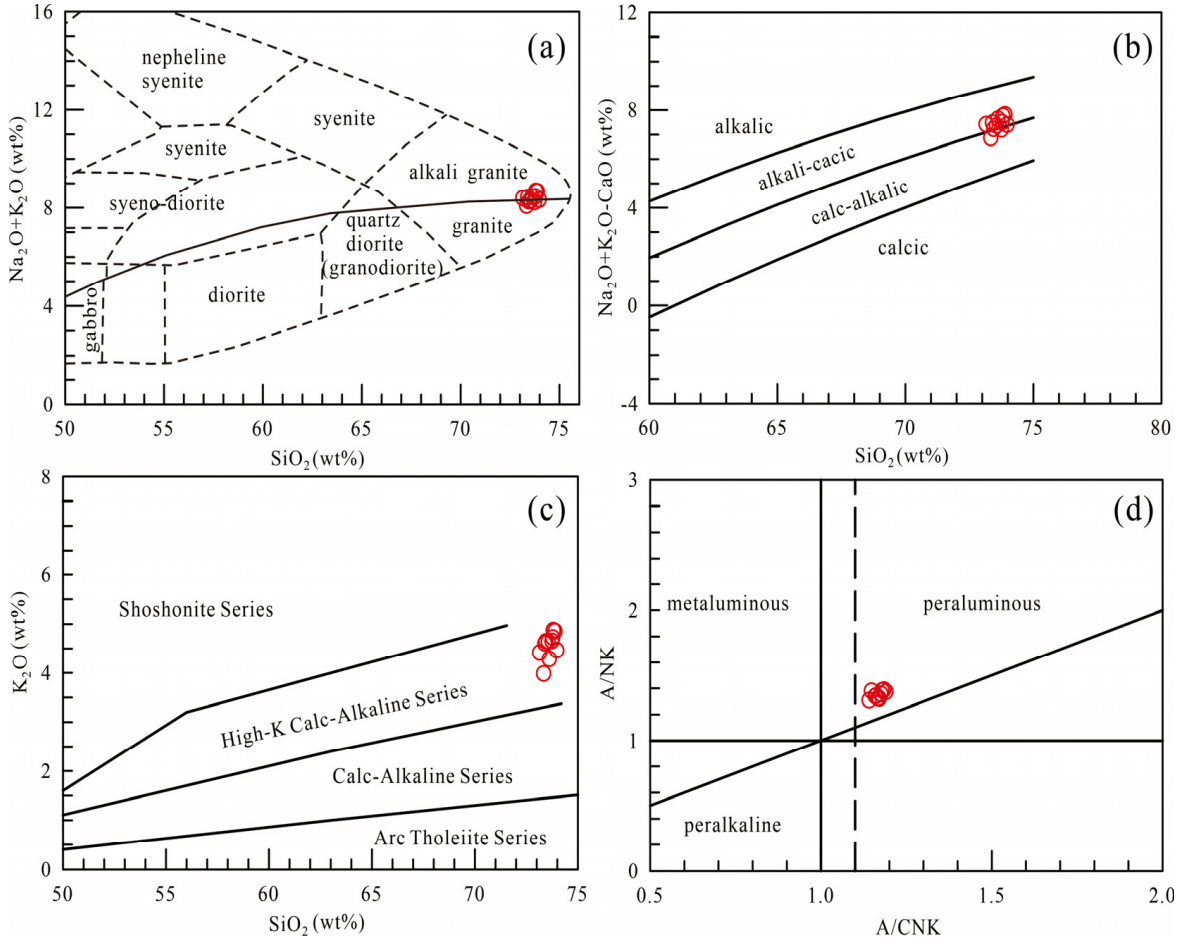

Figure 5. Plots of (**a**) SiO_2 vs. (Na_2O+K_2O) (after [39]), (**b**) SiO_2 vs. (Na_2O+K_2O-CaO) (after [40]), (**c**) SiO_2 vs. K_2O (after [41]); and (**d**) A/CNK vs. A/NK (after [42]) for the LTLG.

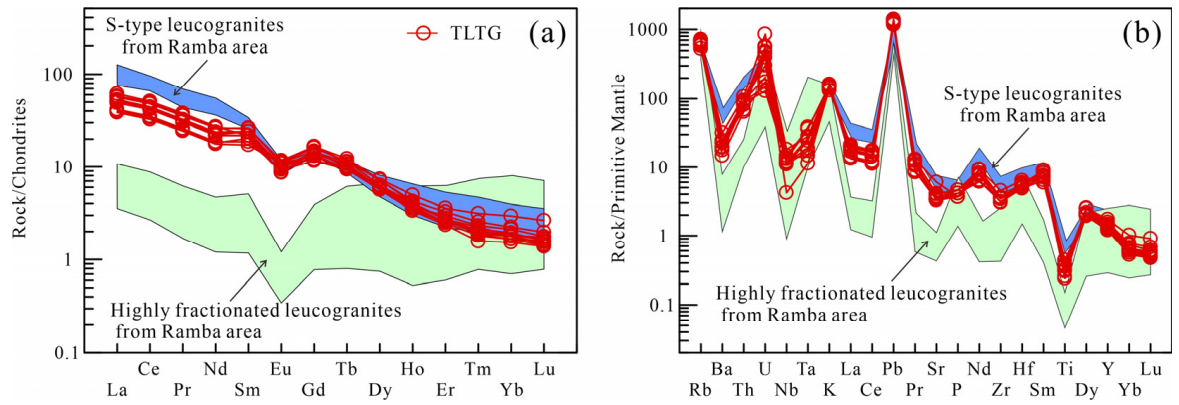

Figure 6. (**a**) REE patterns and (**b**) Spidergrams of the LTLG. The values of chondrite and primitive mantle are from McDonough and Sun [43]. The data of S-type (blue field) and highly fractional (green field) leucogranites from the Ramba area are from Liu et al. [12].

5.3. In Situ Sr-Nd-Hf Isotopic Compositions

5.3.1. Apatite Sr Isotopic Compositions

In situ Sr isotopic analyses of apatite from sample TGL01-4 were conducted, and the results are shown in Table 4 and Figure 7. Eight analyses on eight apatite grains yielded low $^{87}Rb/^{86}Sr$ (0.000101–0.050121, with an average of 0.011120) and high $^{87}Sr/^{86}Sr$

(0.726803–0.728079, with an average of 0.727393) isotopic ratios. The calculated initial $^{87}Sr/^{86}Sr$ ratios (I Sr (t), 0.7268–0.7281) are consistent with analytical $^{87}Sr/^{86}Sr$ values because of the extremely low $^{87}Rb/^{86}Sr$ ratios.

Table 4. In situ and whole-rock Sr-Nd isotopic data of the LTLG.

Sample	$^{87}Rb/^{86}Sr$	$^{87}Sr/^{86}Sr$	2s	I_{Sr} (t)	$^{147}Sm/^{144}Nd$	$^{143}Nd/^{144}Nd$	2s	$^{143}Nd/^{144}Nd(t)$	ε_{Nd} (t)	T_{2DM} (Ga)
Apatite										
Ap01	0.0001	0.727667	0.000337	0.7277	0.3806	0.511911	0.000029	0.511865	−14.6	1.720
Ap02	0.0047	0.726974	0.000284	0.7270	0.3633	0.511957	0.000024	0.511913	−13.7	1.656
Ap03	0.0501	0.728079	0.000288	0.7281	0.3768	0.511982	0.000033	0.511937	−13.2	1.624
Ap04	0.0140	0.726803	0.000427	0.7268						
Ap05	0.0083	0.727367	0.000290	0.7274						
Ap06	0.0025	0.727219	0.000301	0.7272						
Ap07	0.0031	0.727108	0.000350	0.7271						
Ap08	0.0060	0.727930	0.000278	0.7279						
Monazite										
Mz01					0.1216	0.511939	0.000022	0.511924	−13.5	1.641
Mz02					0.1261	0.511953	0.000017	0.511938	−13.2	1.622
Mz03					0.1400	0.511928	0.000020	0.511911	−13.7	1.658
Mz04					0.1324	0.511952	0.000023	0.511936	−13.2	1.625
Mz05					0.1309	0.511940	0.000018	0.511924	−13.5	1.641
Mz06					0.1193	0.511944	0.000017	0.511930	−13.4	1.633
Whole rock *										
LZH1101	17.8085	0.730355	0.000018	0.7257	0.1798	0.511977	0.000010	0.511955	−12.9	1.599
LZH1103	15.3662	0.731090	0.000012	0.7271	0.1901	0.511951	0.000008	0.511928	−13.4	1.635
LZH1107	16.2554	0.731431	0.000010	0.7272	0.1763	0.511950	0.000004	0.511929	−13.4	1.635

* data from [44].

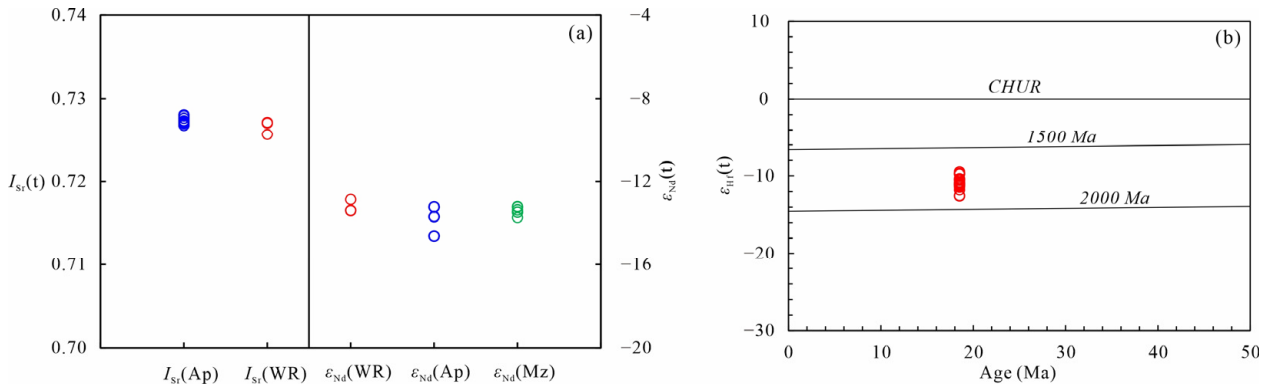

Figure 7. Plots of (**a**) in situ and whole rock Sr-Nd isotopic data and (**b**) Zircon Hf isotopic data of the LTLG.

5.3.2. Apatite and Monazite Nd Isotopic Compositions

In situ Nd isotopic analyses of apatite and monazite from sample TGL01-4 were conducted, and the results are shown in Table 4 and Figure 7. Three analyses on three apatite grains yielded high $^{147}Sm/^{144}Nd$ (0.363255–0.380550, with an average of 0.373521) and low $^{143}Nd/^{144}Nd$ (0.511865–0.511937, with an average of 0.511905) isotopic ratios. Six analyses on six monazite grains showed low $^{147}Sm/^{144}Nd$ (0.119311–0.139963, with an average of 0.128387) and $^{143}Nd/^{144}Nd$ (0.511911–0.511938, with an average of 0.511927) isotopic ratios. The calculated $\varepsilon_{Nd}(t)$ values and two model ages (T_{DM2}) ranged from −14.6 to −13.2 and from 1622 to 1720 Ma, with weighted mean values of −13.6 and 1647 Ma, respectively.

5.3.3. Zircon Hf Isotopic Compositions

Seventeen analyses were conducted across 16 zircon grains (Table 5 and Figure 7). Magmatic grains yielded low $^{176}Hf/^{177}Hf$ (0.282405–0.282493, with an average of 0.282454) and $^{176}Lu/^{177}Hf$ (0.000727–0.002599, with an average of 0.001234) isotopic ratios. The calculated $\varepsilon_{Hf}(t)$ values and two model ages (T_{DM2}) ranged from −12.6 to −9.47 and from 1694 to 1890 Ma, with weighted mean values of −10.9 and 1782 Ma, respectively.

Table 5. In situ Hf isotopic data of zircon from the LTLG.

Spot. No	$^{176}Hf/^{177}Hf$	1σ	$^{176}Lu/^{177}Hf$	1σ	$^{176}Yb/^{177}Hf$	1σ	$^{176}Hf/^{177}Hf(t)$	ε_{Hf} (0)	ε_{Hf} (t)	1σ	T_{DM} (Ma)	T_{DM2} (Ma)
TGL01-4-01	0.282437	0.000013	0.000973	0.000035	0.043089	0.001383	0.282437	−11.9	−11.5	0.4	1151	1819
TGL01-4-02	0.282462	0.000017	0.001315	0.000054	0.056022	0.001598	0.282462	−11.0	−10.6	0.6	1126	1763
TGL01-4-03	0.282455	0.000010	0.000727	0.000008	0.029321	0.000071	0.282455	−11.2	−10.8	0.3	1119	1779
TGL01-4-04	0.282484	0.000010	0.001319	0.000019	0.057886	0.001049	0.282484	−10.2	−9.8	0.4	1095	1715
TGL01-4-05	0.282449	0.000010	0.000769	0.000009	0.028968	0.000103	0.282449	−11.4	−11.0	0.3	1128	1792
TGL01-4-06	0.282442	0.000020	0.001289	0.000012	0.055288	0.000348	0.282442	−11.7	−11.3	0.7	1153	1807
TGL01-4-07	0.282493	0.000014	0.001552	0.000027	0.069375	0.000758	0.282493	−9.9	−9.47	0.5	1089	1694
TGL01-4-08	0.282488	0.000012	0.002599	0.000023	0.125070	0.001412	0.282487	−10.0	−9.67	0.4	1128	1707
TGL01-4-09	0.282447	0.000012	0.001001	0.000011	0.039564	0.000212	0.282447	−11.5	−11.1	0.4	1137	1796
TGL01-4-10	0.282428	0.000022	0.001043	0.000008	0.045795	0.000544	0.282427	−12.2	−11.8	0.8	1166	1840
TGL01-4-11	0.282468	0.000012	0.001532	0.000018	0.066801	0.000760	0.282468	−10.7	−10.4	0.4	1124	1750
TGL01-4-12	0.282445	0.000013	0.001080	0.000010	0.045265	0.000351	0.282445	−11.6	−11.2	0.5	1143	1801
TGL01-4-13	0.282485	0.000014	0.001005	0.000031	0.044787	0.001045	0.282485	−10.1	−9.7	0.5	1084	1712
TGL01-4-14	0.282465	0.000011	0.000843	0.000003	0.037326	0.000143	0.282464	−10.9	−10.5	0.4	1109	1758
TGL01-4-15	0.282407	0.000016	0.000920	0.000006	0.034614	0.000160	0.282406	−12.9	−12.5	0.6	1192	1886
TGL01-4-16	0.282405	0.000010	0.000895	0.000014	0.033825	0.000193	0.282404	−13.0	−12.6	0.3	1194	1890
TGL01-4-17	0.282453	0.000016	0.002122	0.000016	0.084481	0.000409	0.282452	−11.3	−10.9	0.6	1165	1785

6. Discussion

6.1. Genetic Classification of the LTLGs

The genetic classification of granite is often foundational in granite research. I- and S-type granites, proposed by Chappell and White [45], are based on the interpretation of magmatic source rock. I-type granite often originates from meta-igneous rocks, while S-type granite originates from metasedimentary rocks. Loiselle and Wones [46] proposed A-type granite, which is water-poor, moderately alkaline, and originates in a non-orogenic environment from the perspective of geochemistry and tectonic environment. High silica I- and S-type granites sometimes share similar mineralogical and geochemical characteristics with A-type granite, complicating the classifications between I-, S-, and A-type granites [47].

For example, based on our analytical results, the LTLGs have high 10,000 × Ga/Al ratios (>2.6) as a result of their high Ga contents, which could be mistaken for A-type granite [47]. However, all of the LTLGs are corundum-normative and have low Zr, Nb, Ce, Y, and Zn contents and FeO*/MgO, ($Na_2O + K_2O/CaO$) ratios, distinct from A-type granite [48] (Figure 8a,b). Thus, the LTLGs belong to I- or S-type granite. As mentioned in Sections 2 and 4, the LTLGs include aluminous minerals such as muscovite and tourmaline while lacking hornblende and biotite, exhibiting the characteristics of S-type granite. The vast majority of I-type granites are metaluminous and weakly peraluminous, with an A/CNK ratio of less than 1.1 [49]; however, all of the LTLGs are strongly peraluminous with high A/CNK ratios (1.14–1.19), typical of S-type granite. In contrast to I-type granites with high Rb contents (>200 ppm), which have high Th and Y contents that increase with increasing Rb content, S-type granites have low Th and Y contents that decrease as the Rb content increases [50]. As shown in Figure 8c,d, the classic S-type granites of the Interview River Suite in the Lachlan fold belt have low Y and Th contents that decrease with increasing Rb contents. The LTLGs in this study and Ramba S-type leucogranites from the Himalayan belt share similar geochemical characteristics, suggesting a trend in S-type granite evolution. From these observations, it can be concluded that the LTLGs are probably peraluminous S-type leucogranite.

6.2. Petrogenesis of the LTLGs

Peraluminous leucogranites are often considered S-type granites derived from metasedimentary rocks. However, a high degree of magmatic fractionation was recently suggested to have played an important role in the formation of some leucogranites [12,51–56]. Both processes lead to high SiO_2, Al_2O_3, Na_2O, and K_2O and low TiO_2, $Fe_2O_3{}^t$, MgO, CaO, and MnO contents. Peraluminous leucogranites are enriched in Rb, K, and Pb and depleted in Ba, Nb, Zr, and Ti, with negative Eu anomalies, and have high $^{87}Sr/^{86}Sr$ ratios and low $\varepsilon_{Nd}(t)$ and $\varepsilon_{Hf}(t)$ values. Highly fractionated leucogranites have often experienced extensive feldspar differentiation and are thus mostly characterized by significant negative Eu anomalies. In contrast, the TLTGs have relatively limited Eu anomalies (Figure 6), indicating that intensive feldspar fractionation had a negligible role in the formation of the LTLGs. Highly fractionated leucogranites characteristically have relatively low Nb/Ta, Zr/Hf, and

$(La/Yb)_N$ ratios, relatively high Rb/Sr ratios, and significant lanthanide tetrad effects. In contrast, the S-type leucogranites have relatively high Nb/Ta, Zr/Hf, and $(La/Yb)_N$ ratios, relatively low Rb/Sr ratios, and insignificant lanthanide tetrad effects (Figure 9) [57–59]. The TLTGs share similar geochemical characteristics with S-type leucogranites but differ from highly fractionated leucogranites (Figures 6 and 9).

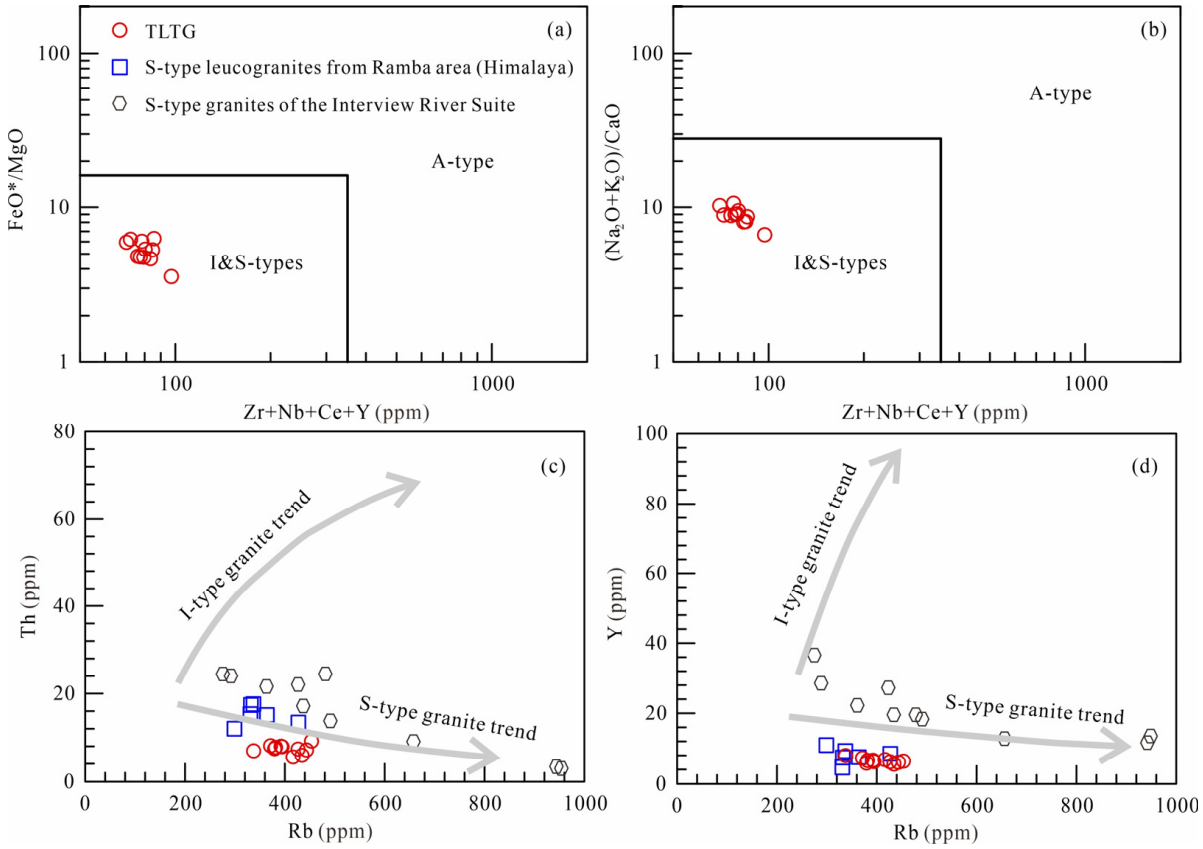

Figure 8. Diagrams of (**a**) (Zr + Nb + Ce + Y) vs. FeO*/MgO (after [48]); (**b**) (Zr + Nb + Ce + Y) vs. $(Na_2O + K_2O)/CaO$ (after [48]); (**c**) Rb vs. Th and (**d**) Rb vs. Y (after [50]) for the LTLG. The data of S-type granites from the Interview River Suite are from Chappell [45]. The data of S-type leucogranites from the Ramba area are from Liu et al. [12].

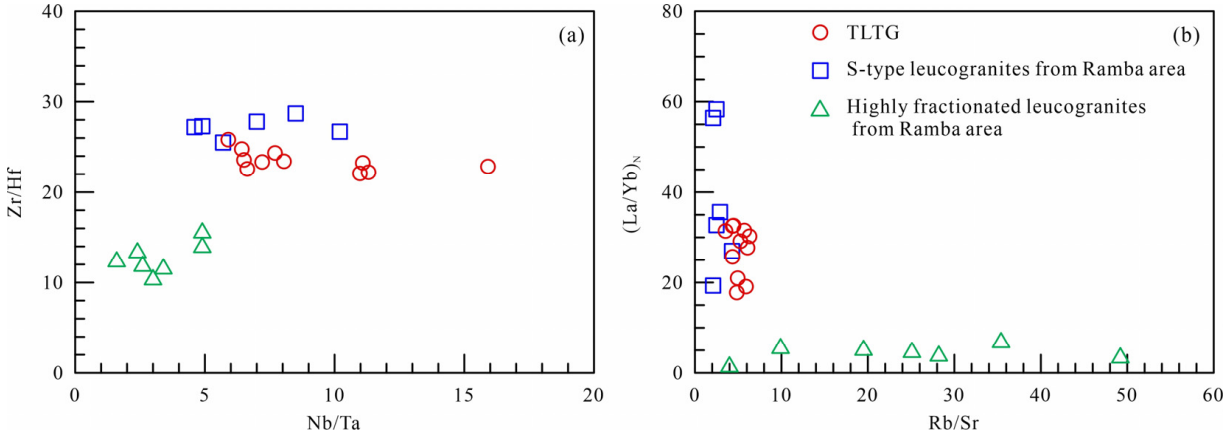

Figure 9. Diagrams of (**a**) Nb/Ta vs. Zr/Hf and (**b**) Rb/Sr vs. $(La/Yb)_N$ for the LTLG. The data of S-type and highly fractional leucogranites from the Ramba area are from Liu et al. [12].

In the ($Na_2O + K_2O + MgO + FeOt + TiO_2$) − ($Na_2O + K_2O$)/($MgO + FeOt + TiO_2$) and ($CaO + MgO + FeOt + TiO_2$) − $CaO/(MgO + FeOt + TiO_2$), discrimination diagrams of the source rock, the LTLG samples plot in the MP field, indicating derivation from a metapelite source (Figure 10a,b). Moreover, the LTLG samples are characterized by low CaO/TiO_2 and high Al_2O_3/TiO_2 ratios, also indicating derivation from crustal metapelites (Figure 10c). As a result of their high Rb/Sr and Rb/Ba ratios, all samples plotted in the field of clay-rich sources in the Rb/Sr-Rb/Ba chemical variation diagrams, further suggesting a metapelite source (Figure 10d).

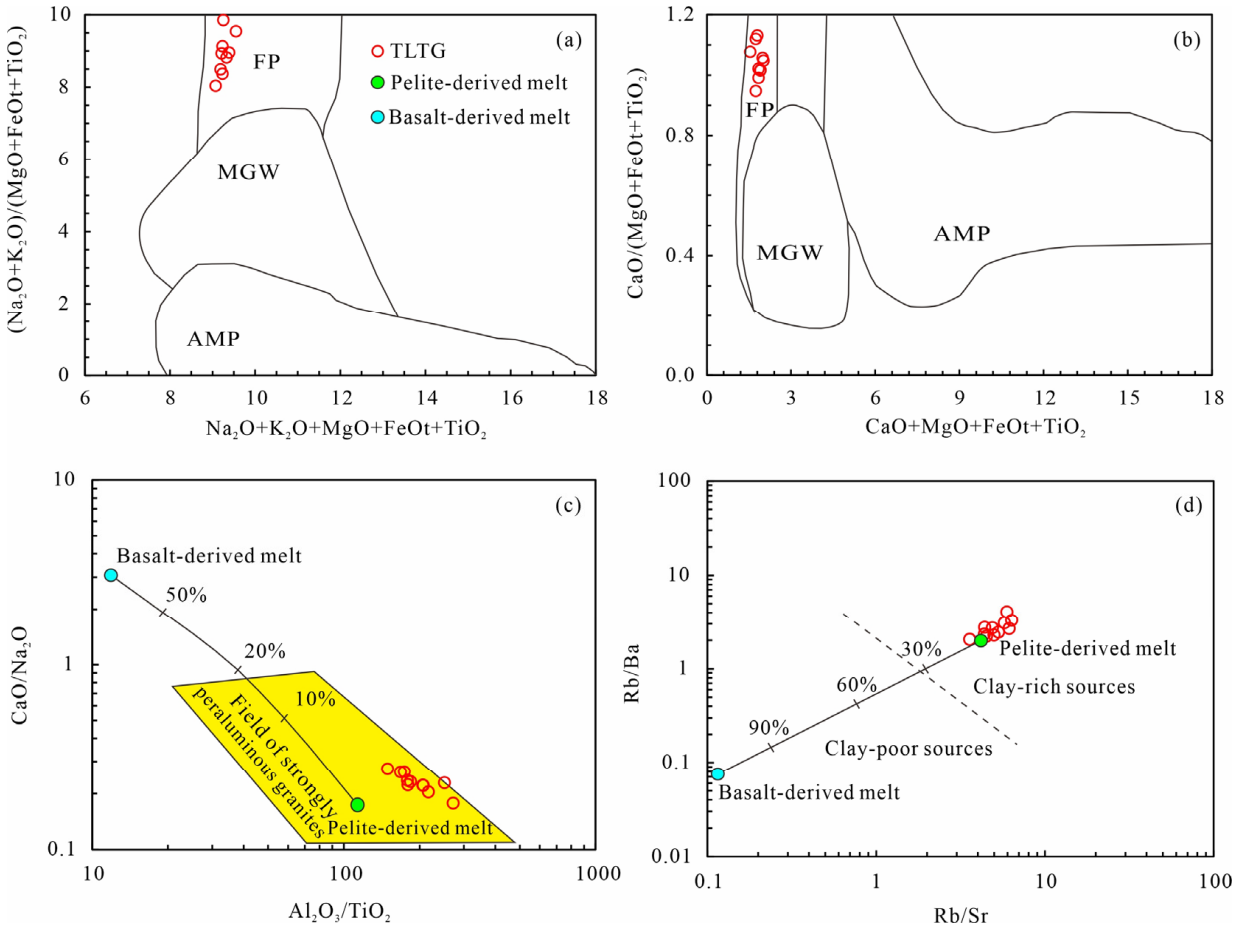

Figure 10. Plots of (**a**) ($Na_2O + K_2O + TiO_2 + TFeO + MgO$) vs. ($Na_2O + K_2O$)/($TiO_2 + TFeO + MgO$) (after [60]), (**b**) ($CaO + TiO_2 + TFeO + MgO$) vs. $CaO/(TiO_2 + TFeO + MgO$) (after [60]), (**c**) Al_2O_3/TiO_2 vs. CaO/TiO_2 (after [61]); and (**d**) Rb/Sr vs. Rb/Ba (after [61]) for the LTLG. MP, metapelites; MGW, metagreywackes; AMP, amphibolites.

Previous studies have shown that peraluminous leucogranites can be produced by fluid-fluxed and fluid-absent melting of a metapelitic source [21,54]. Leucogranites derived from the fluid-fluxed melting of muscovite have relatively higher Sr (>105 ppm), Ba (>305 ppm), and Eu/Eu* (0.7–0.9), but lower Rb (<270 ppm) concentrations and Rb/Sr ratios (<2.2) [5,58]. However, the LTLGs have relatively lower Sr (69.2–86.5 ppm, except for one sample with 127 ppm), Ba (103–222 ppm), and Eu/Eu* (0.49–0.65, except for one sample with 0.76), but higher Rb (338–454 ppm) concentrations and Rb/Sr ratios (3.58–6.35), consistent with results from leucogranites developed through dehydration melting of muscovite (Figure 11).

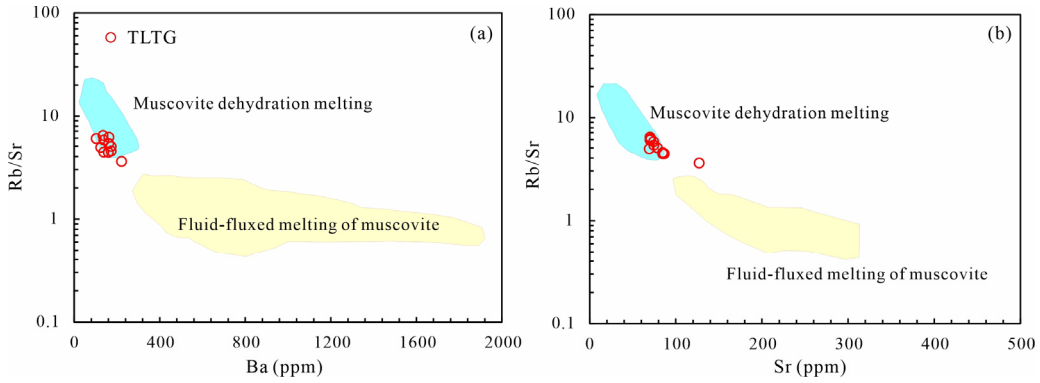

Figure 11. Plots of (**a**) Ba vs. Rb/Sr and (**b**) Sr vs. Rb/Sr (after [62]).

The nature of the Himalayan leucogranite source material is still disputed. Extensive research generally suggests that these leucogranites were derived from the partial melting of the Higher Himalayan Sequence (e.g., [20,63,64]), whereas a two-component mixture between the Higher Himalayan Sequence and Lesser Himalayan Sequence could also be regarded as the source material for the Himalayan leucogranites [17]. Moreover, Liu et al. [58] considered that wall-rock contamination contributed significantly to the development of Ramba garnet-bearing leucogranites. However, the LTLGs exhibit homogeneous Sr, Nd, and Hf isotopic ratios (Figure 7), which differs from the leucogranites reported by Guo and Wilson [17] and Liu et al. [58]. As shown in Figure 12, all of the LTLG samples plot within the Higher Himalayan Sequence field, ruling out the possibility of a two-component mixture between the Higher Himalayan Sequence and the Lesser Himalayan Sequence. In addition, the in situ Sr-Nd isotopic compositions of apatite and monazite are consistent with the whole-rock Sr-Nd isotopic compositions (Figure 7), so wall-rock contamination played a negligible role in forming the LTLGs. Moreover, the TLTGs are characterized by heterogeneous Li contents ranging from 34.1 to 499 ppm and relatively homogeneous Be contents ranging from 11.2 to 21.1 ppm. There is no obvious correlation between the Li and Be contents and the Rb/Sr, Zr/Hf, and Nb/Ta ratios (Figure 13), indicating that the variations in Li and Be contents are not related to magmatic evolution and that the Li content of the parent magma was also heterogeneous. In conclusion, we propose that the LTLGs were derived from muscovite dehydration melting of ancient metapelitic sources from the Higher Himalayan Sequence with negligible wall-rock contamination.

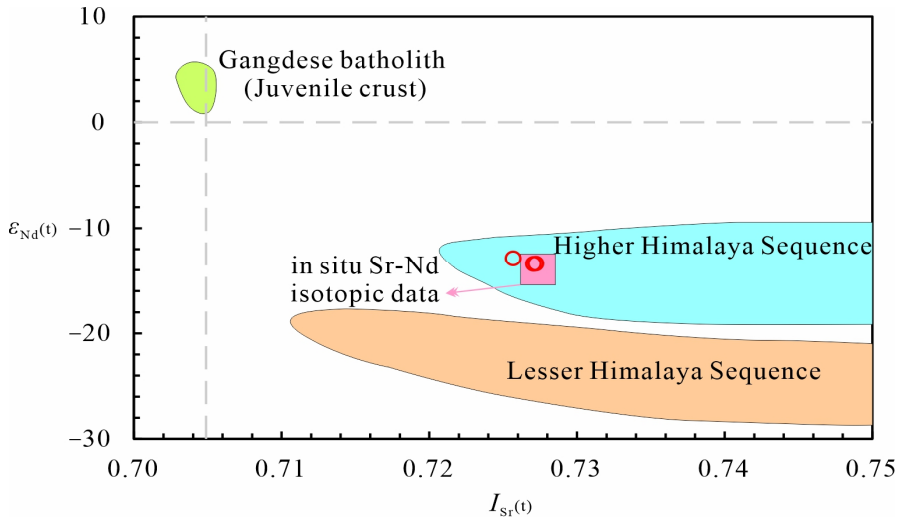

Figure 12. Plots of $\varepsilon_{Nd}(t)$ vs. $I_{Sr}(t)$ for the LTLG. Fields of Gangdese batholith, Higher Himalayan Sequence, and Lesser Himalayan Sequence are from Wu et al. [5].

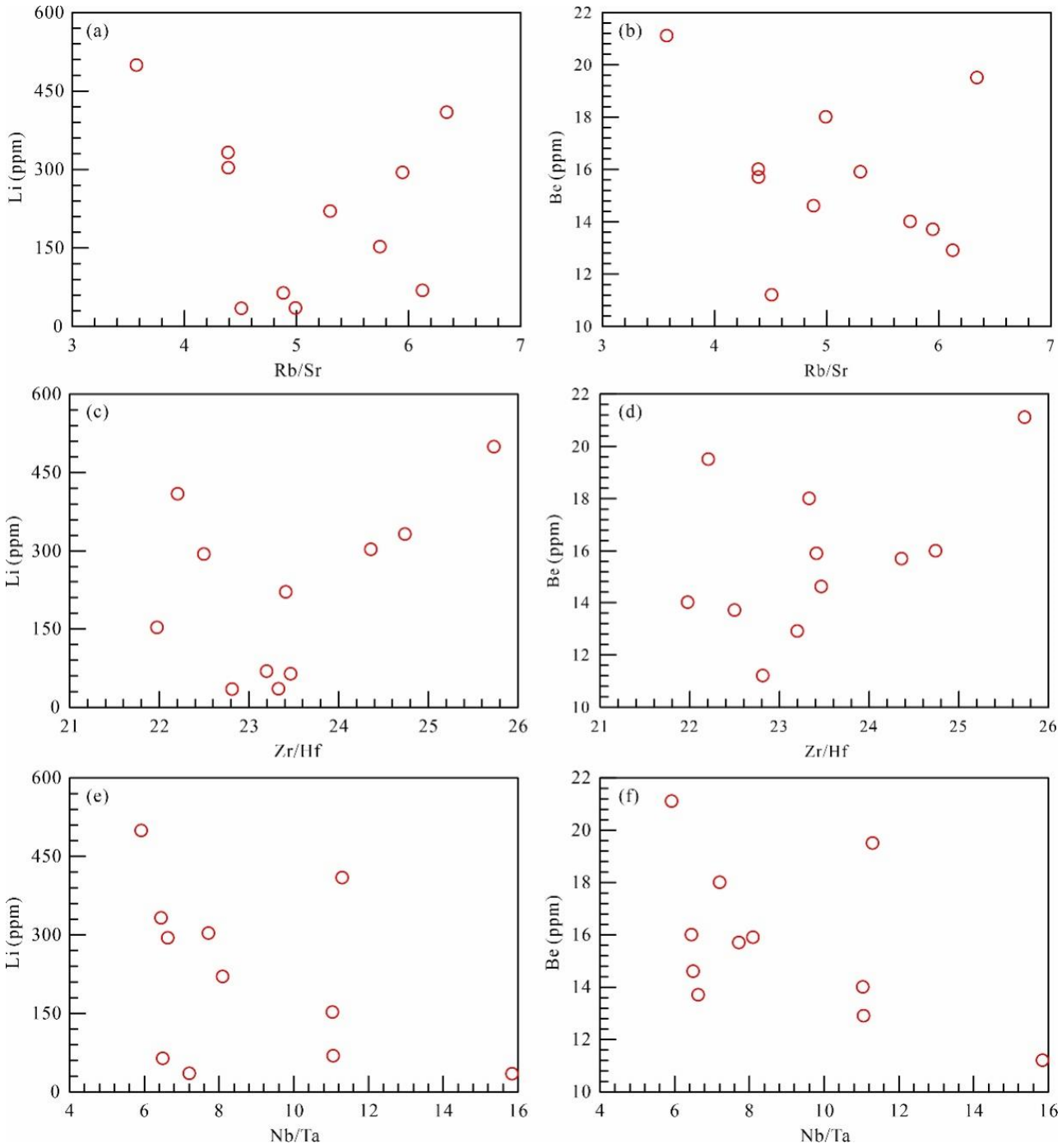

Figure 13. Plots of (**a**) Rb/Sr vs. Li; (**b**) Rb/Sr vs. Be; (**c**) Zr/Hf vs. Li; (**d**) Zr/Hf vs. Be; (**e**) Nb/Ta vs. Li; and (**f**) Nb/Ta vs. Be for the LTLG.

6.3. Tectonic Implications

Himalayan leucogranites were originally regarded as syncollisional granite formed by the partial melting of crustal materials following the India–Asia collision and can be used to recognize the syncollisional environment [65], which contradicts the results of later research that suggests most Himalayan leucogranites were formed in an extensional environment [61]. Many subsequent studies have shown that the geochemical composition of granite has no direct connection to its tectonic background but is often closely related to the composition of the granite's source rock and magmatic evolution [38]. Therefore, a geochemical diagram for identifying the tectonic environment of granite has basically been

abandoned. Numerous U-Pb ages of leucogranites have been reported in the Himalayan belt [66,67]. Recently, Wu et al. [5] divided Himalayan leucogranites into three stages: Eo-Himalayan (46–25Ma), Neo-Himalayan (25–14 Ma), and Post-Himalayan (<14 Ma). All of these leucogranites were formed after the collision between the Indian and Eurasian continents [68]. Eo-Himalayan leucogranites are scarce and have only been reported in the Tethyan Himalayan belt. They characteristically have relatively high Sr contents and Sr/Y ratios, similar to adakitic rocks. They are regarded as products of the partial melting of thickened crustal materials and emplaced during regional compression following the India–Asia collision [58,69,70]. In contrast, Neo-Himalayan and Post-Himalayan leucogranites are widely distributed in both the Tethyan Himalayan and Higher Himalayan belts. Neo-Himalayan and Post-Himalayan leucogranites typically have high Rb/Sr and $^{87}Sr/^{86}Sr$ ratios and are often suggested to have formed in regional extension by activity along the South Tibetan Detachment System (STDS) and N–S-trending rifts, respectively [5,71]. The Neo-Himalayan period, the main period of Himalayan leucogranite formation, is generally characterized by the development of variably deformed leucogranites, while Post-Himalayan leucogranites often lack deformation [72–75]. In the absence of evidence for other heat sources, it is necessary to reduce pressure, which can lead to the partial melting of crustal materials. Activity within the STDS caused a decompression effect that contributed to the extensive melting of crustal materials in the Tethyan Himalayan and Higher Himalayan orogenic belts. Godin et al. [76] systematically summarized the timing of the STDS activity in different regions, which began at ~26, 23, 22, and 23 Ma in the Western Himalaya, Central Western Himalaya, Central Eastern Himalaya, and Eastern Himalaya and lasted until ~16, 13, 16, and 13 Ma, respectively. Zircon and monazite U-(Th)-Pb dating showed that the LTLGs were emplaced at ~19 Ma, consistent with the time of the STDS activity [4,77]. Therefore, we believe that the LTLGs in the Eastern Himalayas were formed by decompression melting in regional extension due to the activity of the STDS. In this study, the average Li and Be contents of the LTLGs were 219 and 15.7 ppm, respectively, which are significantly higher than those of the upper continental crust (24 and 2.1 ppm [78]) and have enormous potential for rare-metal exploration. Moreover, rare-metal mineralization has been discovered in almost all Himalayan leucogranites [24,79–84], and three large or giant rare-metal deposits have been reported [15,22,23,25,85,86], which coincide with the widespread occurrence of Neo-Himalayan leucogranites and the activity of the STDS. Therefore, Himalayan leucogranites have huge potential for rare-metal mineralization in the Himalayan leucogranite belt, and the activity of the STDS likely contributed to the formation of Neo-Himalayan leucogranites and related rare-metal mineralization.

7. Summary of Findings

1. Zircon and monazite dating of tourmaline-bearing leucogranites from the Luozha area in South Tibet yielded identical results, with weighted mean ages of 18.66 ± 0.16 Ma and 18.59 ± 0.22 Ma, respectively.
2. Whole-rock geochemical and in situ Sr-Nd-Hf isotopic data indicate that the tourmaline-bearing leucogranites are characterized by high SiO_2, Al_2O_3, Na_2O, and K_2O contents and A/CNK, Al_2O_3/TiO_2, and Rb/Sr ratios, and low TiO_2, $Fe_2O_3{}^t$, MgO, CaO, and MnO contents and CaO/TiO_2 and Eu/Eu* ratios, typical of S-type granite. The samples analyzed share similar features in their LREE and LILE enrichment and HREE and HFSE depletion, with homogeneous and high I Sr (t) but low $\varepsilon_{Nd}(t)$ and $\varepsilon_{Hf}(t)$.
3. The tourmaline-bearing leucogranites were derived from the muscovite dehydration melting of an ancient metapelitic source within the Higher Himalayan Sequence, and wall-rock contamination played only a negligible role in their formation.
4. The leucogranites were formed in regional extension due to the activity of the STDS, which contributed to the formation of Neo-Himalayan leucogranites and associated rare-metal mineralization.

Author Contributions: Y.D.: Conceptualization, Investigation, Writing—original draft. K.L.: Data curation. Y.L.: Data curation, Resources. J.Z.: Investigation, Resources. C.Y.: Investigation, Writing—original draft, Writing—review & editing, Supervision. G.Z.: Data curation, Resources. R.L.: Formal analysis, Visualization. D.L.: Formal analysis, Visualization. All authors have read and agreed to the published version of the manuscript.

Funding: This study was supported by the key research and development program of Xizang Autonomous Region (Grant No. XZ202201ZY0020G), 2023 Central Government Support Fund for Reform and Development of Local Universities (Second Batch)—Research on Major Engineering Problems and Energy Planning & Construction of Sichuan-Tibet Railway Corridor under the Background of New Engineering (Grant No. 00061146), the Fundamental Research Funds for National Natural Science Foundation of China (Grant No. U21A2015), the Major Science and Technology Project of Xizang Autonomous Region (Grant No. XZ202201ZD0004G), the Second Tibetan Plateau Scientific Expedition and Research Program (Grant No. 2019 QZKK0806).

Data Availability Statement: Data will be made available on request.

Conflicts of Interest: The authors declare that they have no known competing financial interests or personal relationships that could have appeared to influence the work reported in this paper.

References

1. Yin, A.; Harrison, T.M. Geologic evolution of the Himalayan–Tibetan orogen. *Annu. Rev. Earth Planet. Sci.* **2000**, *28*, 211–280. [CrossRef]
2. Yin, A. Cenozoic tectonic evolution of Asia: A preliminary synthesis. *Tectonophysics* **2010**, *488*, 293–325. [CrossRef]
3. Hou, Z.Q.; Qu, X.M.; Yang, Z.S.; Meng, X.J.; Li, Z.Q.; Yang, Z.M.; Zheng, M.P.; Zheng, Y.Y.; Nie, F.J.; Gao, Y.F.; et al. Metallogenesis in Tibetan collisional orogenic belt: III. Mineralization in post-collisional extension setting. *Miner. Depos.* **2006**, *25*, 629–651. (In Chinese with English Abstract).
4. Wu, F.Y.; Liu, Z.C.; Liu, X.C.; Ji, W.Q. Himalayan leucogranite: Petrogenesis and implications to orogenesis and plateau uplift. *Acta Petrol. Sin.* **2015**, *31*, 1–36. (In Chinese with English Abstract).
5. Wu, F.Y.; Liu, X.C.; Liu, Z.C.; Wang, R.C.; Xie, L.; Wang, J.M.; Ji, W.Q.; Yang, L.; Liu, C.; Khanal, G.P.; et al. Highly fractionated Himalayan leucogranites and associated rare-metal mineralization. *Lithos* **2020**, *352*, 105319. [CrossRef]
6. Xu, Z.Q.; Yang, J.S.; Hou, Z.Q.; Zhang, Z.M.; Zeng, L.S.; Li, H.B.; Zhang, J.X.; Li, Z.H.; Ma, X.X. The progress in the study of continental dynamics of the Tibetan Plateau. *Geol. China* **2016**, *43*, 1–42. (In Chinese with English Abstract).
7. Zeng, L.S.; Gao, L.E. Cenozoic crustal anatexis and the leucogranites in the Himalayan collisional orogenic belt. *Acta Petrol. Sin.* **2017**, *33*, 1420–1444. (In Chinese with English Abstract).
8. Deng, J.F.; Zhao, H.L.; Lai, S.C.; Liu, H.X.; Luo, Z.H. Generation of muscovite/two-mica granite and intracontinental subduction. *Earth Sci. J. China Univ. Geosci.* **1994**, *19*, 139–147. (In Chinese with English Abstract).
9. Visonà, D.; Lombardo, B. Two-mica and tourmaline leucogranites from the Everest-Makalu region (Nepal-Tibet). Himalayan leucogranite genesis by isobaric heating? *Lithos* **2002**, *62*, 125–150. [CrossRef]
10. Zhang, J.Y.; Liao, Q.A.; Li, D.W. Geochemical features of the high Himalayan leucogranites of Dingjie Area, Tibet: Implication for magma sources. *Geol. Sci. Technol. Inf.* **2004**, *22*, 9–14. (In Chinese with English Abstract).
11. Guo, S.S.; Li, S.G. Petrological and geochemical constraints on the origin of leucogranites. *Earth Sci. Front.* **2007**, *14*, 290–298.
12. Liu, Z.C.; Wu, F.Y.; Liu, X.C.; Wang, J.G.; Yin, R.; Qiu, Z.L.; Ji, W.Q.; Yang, L. Mineralogical evidence for fractionation processes in the Himalayan leucogranites of the Ramba Dome, southern Tibet. *Lithos* **2019**, *340*, 71–86. [CrossRef]
13. Wang, Z.Z.; Liu, S.A.; Liu, Z.C.; Zheng, Y.C.; Wu, F.Y. Extreme Mg and Zn isotope fractionation recorded in the Himalayan leucogranites. *Geochim. Cosmochim. Acta* **2019**, *278*, 305–321. [CrossRef]
14. Yan, H.; Yu, D.; Wang, S.; Ma, C. Magmatic Garnet and Magma Evolution in Cuonadong Leucogranites: Constraints from Petrology and Mineral Geochemistry. *Minerals* **2022**, *12*, 1275. [CrossRef]
15. Liu, C.; Wang, R.C.; Linnen, R.L.; Wu, F.Y.; Xie, L.; Liu, X.C. Continuous Be mineralization from two-mica granite to pegmatite: Critical element enrichment processes in a Himalayan leucogranite pluton. *Am. Mineral.* **2023**, *108*, 31–41. [CrossRef]
16. Yang, X.S.; Jin, Z.M.; Huenges, E.; Frank, R.S.; Wunder, B. Experimental study on dehydration melting of natural biotite-plagioclase gneiss from high Himalayas and implications for Himalayan crust anatexis. *Chin. Sci. Bull.* **2001**, *46*, 867–872. [CrossRef]
17. Guo, Z.F.; Wilson, M. The Himalayan leucogranites: Constraints on the nature of their crustal source region and geodynamic setting. *Gondwana Res.* **2012**, *22*, 360–376. [CrossRef]
18. Gou, Z.B.; Zhang, Z.M.; Dong, X.; Xiang, H.; Ding, H.X.; Tian, Z.L.; Lei, H.C. Petrogenesis and tectonic implications of the Yadong leucogranites, southern Himalaya. *Lithos* **2016**, *256*, 300–310. [CrossRef]
19. Gao, P.; Zheng, Y.F.; Zhao, Z.F.; Sun, G.C. Source diversity in controlling the compositional diversity of the Cenozoic granites in the Tethyan Himalaya. *Lithos* **2021**, *388*, 106072. [CrossRef]

20. Aoya, M.; Wallis, S.R.; Terada, K.; Lee, J.; Kawakami, T.; Wang, Y.; Heizler, M. North-south extension in the Tibetan crust triggered by granite emplacement. *Geology* **2005**, *33*, 853–856. [CrossRef]
21. King, J.; Harris, N.; Argles, T.; Parrish, R.; Zhang, H.F. Contribution of crustal anatexis to the tectonic evolution of indian crust beneath southern Tibet. *Geol. Soc. Am. Bull.* **2011**, *123*, 218–239. [CrossRef]
22. Li, G.M.; Zhang, L.K.; Jiao, Y.J.; Xia, X.B.; Dong, S.L.; Fu, J.G.; Liang, W.; Zhang, Z.; Wu, J.Y.; Dong, L.; et al. First discovery and implications of Cuonadong superlarge Be-W-Sn polymetallic deposit in Himalayan metallogenic belt, southern Tibet. *Miner. Depos.* **2017**, *36*, 1003–1008. (In Chinese with English Abstract).
23. Qin, K.Z.; Zhao, J.X.; He, C.T.; Shi, R.Z. Discovery of the Qongjiagang giant lithium pegmatite deposit in Himalaya, Tibet, China. *Acta Petrol. Sin.* **2021**, *37*, 3277–3286. (In Chinese with English Abstract).
24. Wu, F.Y.; Wang, R.C.; Liu, X.C.; Xie, L. New breakthroughs in the studies of Himalayan rare-metal mineralization. *Acta Petrol. Sin.* **2021**, *37*, 3261–3276. (In Chinese with English Abstract).
25. Li, G.M.; Fu, J.G.; Guo, W.K.; Zhang, H.; Zhang, L.K.; Dong, S.L.; Li, Y.X.; Wu, J.Y.; Jiao, Y.J.; Jin, C.H.; et al. Discovery of the Gabo granitic pegmatite-type lithium deposit in the Kulagangri Dome, eastern Himalayan metallogenic belt, and its prospecting implication. *Acta Petrol. Mineral.* **2022**, *41*, 1109–1119. (In Chinese with English Abstract).
26. Whitney, D.L.; Evans, B.W. Abbreviations for names of rock-forming minerals. *Am. Mineral.* **2010**, *95*, 185–187. [CrossRef]
27. Liu, Y.S.; Hu, Z.C.; Gao, S.; Günther, D.; Xu, J.; Gao, C.G.; Chen, H.H. In situ analysis of major and trace elements of anhydrous minerals by LA-ICP-MS without applying an internal standard. *Chem. Geol.* **2008**, *257*, 34–43. [CrossRef]
28. Liu, Y.S.; Gao, S.; Hu, Z.C.; Gao, C.G.; Zong, K.Q.; Wang, D.B. Continental and oceanic crust recycling-induced melt-peridotite interactions in the Trans-North China Orogen: U-Pb dating, Hf isotopes and trace elements in zircons of mantle xenoliths. *J. Petrol.* **2010**, *51*, 537–571. [CrossRef]
29. Ludwig, K.R. *A Geochronological Toolkit for Microsoft Excel*; Isoplot: Berkeley, CA, USA, 2003; pp. 1–77.
30. *GB/T 14506.30-2010*; General Administration of Quality Supervision, Inspection and Quarantine of the People's Republic of China and Standardization Administration of the People's Republic of China. Methods for Chemical Analysis of Silicate Rocks—Part 30: Determination of 44 Elements. Standards Press of China: Beijing, China, 2010; 14p.
31. Zhang, W.; Hu, Z.; Spectroscopy, A. Estimation of Isotopic Reference Values for Pure Materials and Geological Reference Materials. *At. Spectrosc.* **2020**, *41*, 93–102. [CrossRef]
32. Tong, X.R.; Liu, Y.S.; Hu, Z.C.; Chen, H.H.; Zhou, L.; Hu, Q.H.; Xu, R.; Deng, L.X.; Chen, C.F.; Yang, L.; et al. Accurate determination of Sr isotopic compositions in clinopyroxene and silicate glasses by LA-MC-ICP-MS. *Geostand. Geoanalytical Res.* **2016**, *40*, 85–99. [CrossRef]
33. Zhang, W.; Hu, Z.; Liu, Y.; Wu, T.; Deng, X.; Guo, J.; Han, Z. Improved in situ Sr isotopic analysis by a 257 nm femtosecond laser in combination with the addition of nitrogen for geological minerals. *Chem. Geol.* **2018**, *479*, 10–21. [CrossRef]
34. Yang, Y.H.; Wu, F.Y.; Yang, J.H.; Chew, D.M.; Xie, L.W.; Chu, Z.Y.; Zhang, Y.B.; Huang, C. Sr and Nd isotopic compositions of apatite reference materials used in U-Th-Pb geochronology. *Chem. Geol.* **2014**, *385*, 35–55. [CrossRef]
35. Xu, L.; Hu, Z.C.; Zhang, W.; Yang, L.; Liu, Y.S.; Gao, S. In situ Nd isotope analyses in geological materials with signal enhancement and non-linear mass dependent fractionation reduction using laser ablation MC-ICP-MS. *J. Anal. At. Spectrom.* **2015**, *30*, 232–244. [CrossRef]
36. Wu, Y.B.; Zheng, Y.F. Genesis of zircon and its constraints on interpretation of U-Pb age. *Chin. Sci. Bull.* **2004**, *49*, 1554–1569. [CrossRef]
37. Watson, E.B.; Wark, D.A.; Thomas, J.B. Crystallization thermometers for zircon and rutile. *Contrib. Mineral. Petrol.* **2006**, *151*, 413–433. [CrossRef]
38. Watson, E.B.; Harrison, T.M. Zircon saturation revisited: Temperature and composition effects in a variety of crustal magma types. *Earth Planet. Sci. Lett.* **1983**, *64*, 295–304. [CrossRef]
39. Wilson, M. *Igneous Petrogenesis: A Global Tectonic Approach*; Unwin Hyman: London, UK, 1989; 466p.
40. Frost, B.R.; Barnes, C.G.; Collins, W.J.; Arculus, R.J.; Ellis, D.J.; Frost, C.D. A geochemical classification for granitic rocks. *J. Petrol.* **2001**, *42*, 2033–2048. [CrossRef]
41. Peccerillo, A.; Taylor, S.R. Geochemistry of Eocene calc-alkaline volcanic rocks from the Kastamonu area, northern Turkey. *Contrib. Mineral. Petrol.* **1976**, *58*, 63–81. [CrossRef]
42. Maniar, P.D.; Piccoli, P.M. Tectonic discrimination of granitoids. *Geol. Soc. Am. Bull.* **1989**, *101*, 635–643. [CrossRef]
43. MDonough, W.F.; Sun, S.S. Composition of the Earth. *Chem. Geol.* **1995**, *120*, 223–253. [CrossRef]
44. Huang, C.M.; Zhao, Z.D.; Zhu, D.C.; Liu, D.; Huang, Y.; Dong, M.C.; Hu, Z.C.; Zheng, J.P. Geochemistry, zircon U-Pb chronology and Hf isotope of Luozha leucogranite, southern Tibet: Implication for petrogenesis. *Acta Petrol. Sin.* **2013**, *29*, 3689–3702.
45. Chappell, B.W.; White, A. Two contrasting granite types. *Pac. Geol.* **1974**, *8*, 173–174.
46. Loiselle, M.C.; Wones, D.R. Characteristics of Anorogenic Granites. *Geol. Soc. Am. Abstr. Programs* **1979**, *11*, 468.
47. Wu, F.Y.; Li, X.H.; Yang, J.H.; Zheng, Y.F. Discussion on the petrogenesis of granites. *Acta Petrol. Sin.* **2007**, *23*, 1217–1238. (In Chinese with English Abstract).
48. Whalen, J.B.; Currie, K.L.; Chappell, B.W. A-type granites: Geochemical characteristics, discrimination and petrogenesis. *Contrib. Mineral. Petrol.* **1987**, *95*, 407–419. [CrossRef]
49. Chappell, B.W. Aluminium saturation in I-and S-type granites and the characterization of fractionated haplogranites. *Lithos* **1999**, *46*, 535–551. [CrossRef]

50. Li, X.H.; Li, W.X.; Li, Z.X. On genetic types and tectonic significance of early Yanshanian granites in Nanling. *Chin. Sci. Bull.* **2007**, *9*, 981–991.
51. Acosta-Vigil, A.; London, D.; Morgan, V.I. Experiments on the kinetics of partial melting of a leucogranite at 200 MPa H_2O and 690–800 °C: Compositional variability of melts during the onset of H_2O-saturated crustal anatexis. *Contrib. Mineral. Petrol.* **2006**, *151*, 539–557. [CrossRef]
52. Searle, M.P.; Cottle, J.M.; Streule, M.J.; Waters, D.J. Crustal melt granites and migmatites along the Himalaya: Melt source, segregation, transport and granite emplacement mechanisms. *Earth Environ. Sci. Trans. R. Soc. Edinb.* **2009**, *100*, 219–233. [CrossRef]
53. Teixeira, R.J.S.; Neiva, A.M.R.; Gomes, M.E.P.; Corfu, F.; Cuesta, A.; Croudace, I.W. The role of fractional crystallization in the genesis of early syn-D3, tin-mineralized Variscan two-mica granites from the Carrazeda de Ansiães area, northern Portugal. *Lithos* **2012**, *153*, 177–191. [CrossRef]
54. Gao, L.E.; Zeng, L.S. Fluxed melting of metapelite and the formation of Miocene high-CaO two-mica granites in the Malashan gneiss dome, southern Tibet. *Geochim. Cosmochim. Acta* **2014**, *130*, 136–155. [CrossRef]
55. Huang, F.; Bai, R.; Deng, G.; Liu, X.; Li, X. Barium isotope evidence for the role of magmatic fluids in the origin of Himalayan leucogranites. *Sci. Bull.* **2021**, *66*, 2329–2336. [CrossRef] [PubMed]
56. Gao, L.E.; Zeng, L.; Zhao, L.; Yan, L. Sequential melting of deep crustal source rocks in a rift system: An example from southern Tibet. *Chem. Geol.* **2023**, *618*, 121295. [CrossRef]
57. Wu, F.Y.; Sun, D.Y.; Li, H.; Jahn, B.M.; Wilde, S. A-type granites in northeastern China: Age and geochemical constraints on their petrogenesis. *Chem. Geol.* **2002**, *187*, 143–173. [CrossRef]
58. Liu, Z.C.; Wu, F.Y.; Ji, W.Q.; Wang, J.G.; Liu, C.Z. Petrogenesis of the Ramba leucogranite in the Tethyan Himalaya and constraints on the channel flow model. *Lithos* **2014**, *208*, 118–136. [CrossRef]
59. Liu, Z.C.; Liu, X.C.; Yu, L.J.; Wang, J. Highly fractionated origin and magmatic-hydrothermal evolution of the Kampa leucogranites in the Tethyan Himalaya. *J. Nanjing Univ. Nat. Sci.* **2020**, *56*, 800–814. (In Chinese with English Abstract).
60. Kaygusuz, A.; Siebel, W.; Şen, C.; Satir, M. Petrochemistry and petrology of I-type granitoids in an arc setting: The composite Torul pluton, Eastern Pontides, NE Turkey. *Int. J. Earth Sci.* **2008**, *97*, 739–764. [CrossRef]
61. Sylvester, P.J. Post-collisional strongly peraluminous granites. *Lithos* **1998**, *45*, 29–44. [CrossRef]
62. Gao, L.E.; Zeng, L.S.; Asimow, P.D. Contrasting geochemical signatures of fluidabsent versus fluid-fluxed melting of muscovite in metasedimentary sources: The Himalayan leucogranites. *Geology* **2017**, *45*, 39–42. [CrossRef]
63. Richards, A.; Parrish, R.; Harris, N.; Argles, T.; Zhang, L. Correlation of lithotectonic units across the eastern Himalaya, Bhutan. *Geology* **2006**, *34*, 341–344. [CrossRef]
64. Zeng, L.S.; Gao, L.E.; Tang, S.H.; Hou, K.J.; Guo, C.L.; Hu, G.Y. Eocene magmatism in the Tethyan Himalaya, Southern Tibet. *Geol. Soc. Spec. Publ.* **2014**, *412*, 287–316. [CrossRef]
65. Pearce, J.A.; Harris, N.B.; Tindle, A.G. Trace element discrimination diagrams for the tectonic interpretation of granitic rocks. *J. Petrol.* **1984**, *25*, 956–983. [CrossRef]
66. Cao, H.W.; Pei, Q.M.; Santosh, M.; Li, G.M.; Zhang, L.K.; Zhang, X.F.; Zhang, Y.H.; Zou, H.; Dai, Z.W.; Lin, B.; et al. Himalayan leucogranites: A review of geochemical and isotopic characteristics, timing of formation, genesis, and rare metal mineralization. *Earth-Sci. Rev.* **2022**, *234*, 104229. [CrossRef]
67. Liu, H.; Li, W.; Cao, H.; Zhang, X.; Li, Y.; Gao, K.; Dong, L.; Zhang, K.; Liu, X. Origin of Himalayan Eocene Adakitic Rocks and Leucogranites: Constraints from Geochemistry, U-Pb Geochronology and Sr-Nd-Pb-Hf Isotopes. *Minerals* **2023**, *13*, 1204. [CrossRef]
68. Hu, X.M.; Garzanti, E.; Wang, J.G.; Huang, W.T.; Wei, A.; Webb, A. The timing of India-Asia collision onset—Facts, theories, controversies. *Earth Sci. Rev.* **2016**, *160*, 264–299. [CrossRef]
69. Zeng, L.S.; Gao, L.E.; Xie, K.J.; Jing, L.Z. Mid-Eocene high Sr/Y granites in the Northern Himalayan Gneiss Domes: Melting thickened lower continental crust. *Earth Planet. Sci. Lett.* **2011**, *303*, 251–266. [CrossRef]
70. Hou, Z.Q.; Zheng, Y.C.; Zeng, L.S.; Gao, L.E.; Huang, K.X.; Li, W.; Li, Q.Y.; Fu, Q.; Liang, W.; Sun, Q.Z. Eocene-Oligocene granitoids in southern Tibet: Constraints on crustal anatexis and tectonic evolution of the Himalayan orogen. *Earth Planet. Sci. Lett.* **2012**, *349*, 38–52. [CrossRef]
71. Hodges, K.V. Tectonics of the Himalaya and southern Tibet from two perspectives. *Geol. Soc. Am. Bull.* **2000**, *112*, 324–350. [CrossRef]
72. Zhang, H.F.; Harris, N.; Parrish, R.; Zhang, L.; Zhao, Z.D. U–Pb ages of Kude and Sajia leucogranites in Sajia dome from north Himalaya and their geological implications. *Chin. Sci. Bull.* **2004**, *49*, 2087–2092. [CrossRef]
73. Zhang, L.K.; Zhang, Z.; Li, G.M.; Dong, S.L.; Xia, X.B.; Liang, W.; Fu, J.G.; Cao, H.W. Rock assemblage, structural characteristics and genesis mechanism of the Cuonadong dome, Tethys Himalaya. *Earth Sci.* **2018**, *43*, 2664–2683. (In Chinese with English Abstract).
74. Larson, K.P.; Godin, L.; Davis, W.J.; Davis, D.W. Out-of-sequence deformation and expansion of the Himalayan orogenic wedge: Insight from the Changgo culmination, south Central Tibet. *Tectonics* **2010**, *29*, 1–30. [CrossRef]
75. Wang, J.M.; Wu, F.Y.; Rubatto, D.; Liu, K.; Zhang, J.J.; Liu, X.C. Early Miocene rapid exhumation in southern Tibet: Insights from P–T–t–D–magmatism path of Yardoi dome. *Lithos* **2018**, *30*, 38–56. [CrossRef]
76. Godin, L.; Grujic, D.; Law, R.D.; Searle, M.P. *Channel Flow, Ductile Extrusion and Exhumation in Continental Collision Zones: An Introduction*; Special Publications: London, UK, 2008; pp. 1–23.

77. Wang, X.X.; Zhang, J.J.; Liu, J.; Yan, S.Y.; Wang, J.M. Middle-Miocene transformation of tectonic regime in the Himalayan orogen. *Chin. Sci. Bull.* **2013**, *58*, 108–117. [CrossRef]
78. Rudnick, R.L.; Gao, S. *Composition of the Continental Crust*; Holland, H.D., Turekian, K.K., Eds.; Elsevier: Oxford, UK, 2014; pp. 1–51.
79. Gao, L.E.; Zeng, L.S.; Hu, G.Y.; Gao, J.H.; Zhao, L.H.; Wang, Y.Y. Rare Metal Enrichment in Leucogranite within Nariyongcuo Gneiss Dome, South Tibet. *Earth Sci.* **2019**, *44*, 1860–1875.
80. He, C.T.; Qin, K.Z.; Li, A.; Zhou, Q.F.; Zhao, J.X.; Li, G.M. Preliminary study on occurrence status of berylium andgenetic mechanism in Cuonadong tungsten-tin-beryllium deposit, eastern Himalaya. *Acta Petrol. Sin.* **2020**, *36*, 3593–3606.
81. Zhao, J.X.; He, C.T.; Shi, R.Z.; Qin, K.Z.; Yu, K.L.; Qiu, J.T.; Li, Z.; Zhou, Q.F. Mineralogical characteristics of the leucogranite-pegmatite in the Yardoi Gneiss Dome, Himalaya, Tibet: Implication to the rare-metal mineralization. *Acta Petrol. Sin.* **2022**, *38*, 1981–2002.
82. Zhou, W.; Xie, L.; Wang, R.C.; Wu, F.Y.; Tian, E.N.; Liu, C.; Liu, X.C. The study on the micas in the Gyirong leucogranite-pegmatite from Himalaya: Implications for the lithium enrichment. *Acta Petrol. Sin.* **2022**, *38*, 2153–2173.
83. Fu, J.G.; Li, G.M.; Wang, G.; Guo, W.K.; Dong, S.L.; Li, Y.; Zhang, H.; Liang, W.; Jiao, Y. Geochemical Evidence for Genesis of Nb–Ta–Be Rare Metal Mineralization in Highly Fractionated Leucogranites at the Lalong Dome, Tethyan Himalaya, China. *Minerals* **2023**, *13*, 1456. [CrossRef]
84. Zhou, Q.F.; Qin, K.Z.; Liu, Y.C.; He, C.T.; Zhao, J.X.; Li, J.Y.; Zhu, L.O.; Zhao, Y.N.; Zhang, X. Cassiterite of the Kuqu spodumene-bearing pegmatites in the eastern Himalaya, Tibet, and its implication. *Acta Petrol. Sin.* **2024**, *40*, 433–449. (In Chinese with English Abstract). [CrossRef]
85. Cao, H.W.; Li, G.M.; Zhang, R.Q.; Zhang, Y.H.; Zhang, L.K.; Dai, Z.W.; Xia, X.B. Genesis of the Cuonadong tin polymetallic deposit in the Tethyan Himalaya: Evidence from geology, geochronology, fluid inclusions and multiple isotopes. *Gondwana Res.* **2021**, *92*, 72–101. [CrossRef]
86. Fu, J.G.; Li, G.M.; Guo, W.K.; Zhang, H.; Zhang, L.K.; Dong, S.L.; Zhou, L.M.; Li, Y.X.; Jiao, Y.J.; Shi, H.Z. Mineralogical characteristics of columbite group minerals and its implications for magmatic-hydrothermal transition in the Gabo lithium deposit, Himalayan metallogenic belt. *Earth Sci. Front.* **2023**, *30*, 134–150. (In Chinese with English Abstract).